REPORT DOCUMENTATION PAGE

Form Approved
OMB No. 0704-0188

1. AGENCY USE ONLY (Leave Blank)	2. REPORT DATE	3. REPORT TYPE AND DATES COVERED
	6/25/99	Final Technical 6/1/95 - 5/31/99

4. TITLE AND SUBTITLE

Silicon-Based Nanostructures: Experiment & Modeling

5. FUNDING NUMBERS

N00014-95-1-0918

6. AUTHORS

David K. Ferry

7. PERFORMING ORGANIZATION NAME(S) AND ADDRESS(ES)

Arizona State University
Dept. of Electrical Engineering
Tempe, AZ 85287-5706

8. PERFORMING ORGANIZATION REPORT NUMBER

9. SPONSORING / MONITORING AGENCY NAME(S) AND ADDRESS(ES)

Office of Naval Research
800 North Quincy Street
Arlington, VA 22217-5660

10. SPONSORING / MONITORING AGENCY REPORT NUMBER

11. SUPPLEMENTARY NOTES

12a. DISTRIBUTION / AVAILABILITY STATEMENT

Approved for Public Release; distribution is Unlimited

12b. DISTRIBUTION CODE

13. ABSTRACT (Maximum 200 words)

Under this program, research was carried out in the area of Si-based nanoelectronic devices. The primary device of interest was a single-electron tunneling transistor fabricated in the Si MOS system. As part of the program, extended work on chemically-enhanced vapor etching as a tool for lithography and material processing, and upon the processing of $CoSi_2$ as a viable interconnect, were pursued. Theoretical work addressed both the transport in the Si devices as well as the more general problems in small quantum, confined systems. It was natural to apply these results to GaAs based systems as well. Other portions of the effort entailed high-resolution TEM as a routine tool during our materials and device studies and the development of special visualization tools for the theoretical program. Sub-contracts were to SRA, Inc., for quantum transport studies of quantum devices, and for process modeling, and to Los Alamos National Laboratory for similar studies and for visualization of processing

14. SUBJECT TERMS

15. NUMBER OF PAGES
65

16. PRICE CODE

17. SECURITY CLASSIFICATION OF REPORT	18. SECURITY CLASSIFICATION OF THIS PAGE	19. SECURITY CLASSIFICATION OF ABSTRACT	20. LIMITATION OF ABSTRACT
Unclassified	Unclassified	Unclassified	UL

NSN 7540-01-280-5500

Standard Form 298 (Rev. 2-89)
Prescribed by ANSI Std. Z39-1
298-102

Si-Based Nanostructures

Final Report

N00014-95-1-0918

Arizona State University

July 1, 1999

Project Summary

Under this program, research was carried out in the area of Si-based nanoelectronic devices. The primary device of interest was a single-electron tunneling transistor fabricated in the Si MOS system. As part of the program, extended work on chemically-enhanced vapor etching as a tool for lithography and material processing, and upon the processing of $CoSi_2$ as a viable interconnect, were pursued. Theoretical work addressed both the transport in the Si devices as well as the more general problems in small quantum, confined systems. It was natural to apply these results to GaAs based systems as well. Other portions of the effort entailed high-resolution TEM as a routine tool during our materials and device studies and the development of special visualization tools for the theoretical program. Sub-contracts were to SRA, Inc., for quantum transport studies of quantum devices, and for process modeling, and to Los Alamos National Laboratory for similar studies and for visualization of processing.

Contents

1. Single-Electron Tunneling Spectroscopy of Silicon Quantum Dots (Prof. D. K. Ferry, Arizona State University)

We have fabricated a silicon quantum dot embedded in a metal-oxide-semiconductor field effect transistor structure. Two side-gates deplete the quasi-two-dimensional electron gas created by a top inversion gate. We have tested devices ranging in size from 40 to 200 nm. By varying the density with the top gate, the conductance peaks reveal the details of the energy level structure within the dot and their interactions with one another.

There is considerable interest in quantum dots, as they represent the ultimate reduction in the dimensionality of a semiconductor device. In addition, it is hoped that these devices can extend the observations of single-electron tunneling [1] into the semiconductor device realm where they can be coupled to normal transistors. While there have been several observations of single-electron behavior in GaAs heterostructures, efforts in Si-based devices have been limited to either lithographically defined dots [2,3], or devices which have relied upon accidental definition of dots [4,5]. Here, we describe the fabrication and measurements of a dual gate-defined quantum dot which is embedded within a Si metal-oxide-semiconductor field-effect transistor. The dot is formed in the inversion layer created by the top gate, with its lateral definition being provided by two side gates embedded within the gate oxide.

1.1 Device Fabrication

The device is fabricated in a normal manner, with a thermal first oxide 9 nm thick. The lateral side-gates are deposited Cr and a second 50 nm oxide is deposited by plasma enhanced, chemical vapor deposition, upon which the top gate is defined by electron beam lithography. Details of the fabrication procedure have been given elsewhere [6]. A schematic of the device is shown in the inset to Fig. 1.1. Measurements were performed in helium at 4.2 K. All measurements presented in this letter were DC measurements done on an HP4156B semiconductor parameter analyzer. In Fig. 1.1, we plot the drain current through the dot as a

function of the source-drain bias for two values of the gate bias. There is a clear Coulomb blockade present, and this blockade is readily varied by the gate potentials.

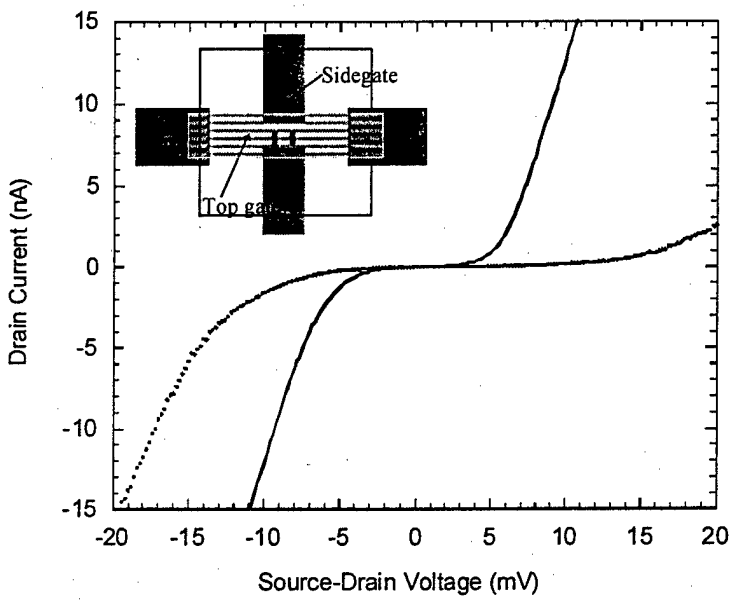

Fig. 1.1 The drain current as a function of source-drain bias for the dot in the Coulomb blockade regime. The solid curve is for $V_g = 2.8$ V, $V_{sg} = -300$, while the dotted curve is for $V_g = 2.9$ V, $V_{sg} = -400$. Increasing the magnitude $V_g - V_{sg}$ appears to increase the confinement of the carriers in the dot. In the inset, we show the structure of the double gates.

1.2 Results

In Fig. 1.2(a), we plot the drain current through the device for a drain bias of 0.2 mV. The family of curves is generated by changing the top gate voltage in 20 mV steps, in the range from 2.5-3.1 V, and sweeping the side-gate voltage from +100 mV to -500 mV. It was found that this measurement sequence was the best for eliminating hysterisis arising from a discrete change in the number of electrons in the dot from run to run. Measurements done with the side gate voltage swept in the opposite direction contained considerable hysterisis which made the interpretation more difficult. The choice of sweep direction does not alter the characteristic but only translates it to the left or right. From this figure, it is clear that the side gate voltage sweep is

depleting the electrons from the dot, and that the current peaks correspond to single-electron events, with the dot being ultimately completely depleted for sufficiently negative side gate voltage, and this threshold is dependent upon the top gate voltage as well. We may assume that the dot is pinched off at the largest negative side gate bias. There is a general linear trend in the position of the peaks. If we look at the first peak from the left, we observe at first a modulation of the peak amplitude with the top gate voltage. However, at higher top gate voltages, the peak splits into multiple peaks. We also observe peaks merging together and splitting apart at different top gate voltages. For example, if we track the shoulder indicated arrow "A", we see that the peaks start to collapse into one large peak and later split up again at more positive gate biases. This is reminiscent of the crossings and anti-crossings in the magneto-electric band structure of a quantum dot [7], except that here the inversion gate is inducing this behavior. To the left of this shoulder, another series of peaks are marked by arrow "B". These are observed to merge together at about the same top gate voltage where peak "A" collapsed, and split again at about the same higher top gate voltage.

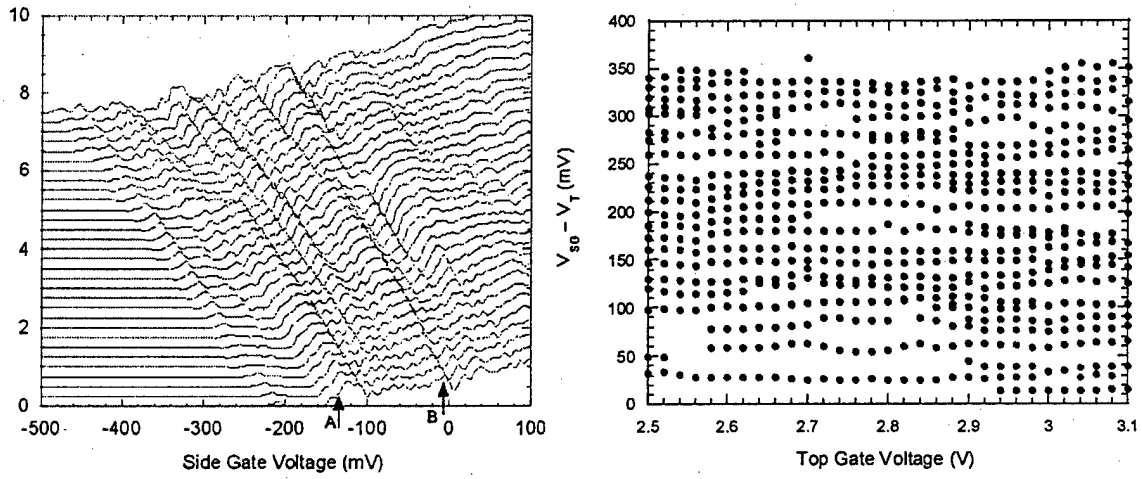

Fig. 1.2 (a) The drain current for fixed drain bias of 0.2 mV. The top gate bias is 2.5 V for the lowest curve and increases by 20 mV per curve up to 3.1 V. Each curve is offset by 0.25 nA. (b) The peak positions after correcting for a threshold voltage V_{th} that indicates the onset of coulomb oscillations. This correction aligns the peaks to help visualization.

In classical coulomb blockade, the spacing between the peaks is a constant equal to q/C_g where C_g is the capacitance from the dot to the gate. However, in semiconductor quantum dots, energy level quantization occurs readily due to a smaller effective mass and a considerably smaller number of electrons in the dot. Thus, when energy level spacing becomes comparable to the coulomb blockade energy, the structure of the peaks reveals a spectroscopic picture of the dot [8]. We believe that size of the dot is much smaller than the lithographically defined 200 nm for the measurements shown in Fig. 1.2(a), and the effective dot size may be smaller than 20 nm. This can be deduced by estimating the capacitance from the coulomb gap and obtaining an upper limit on the size from self-capacitance estimates of the dot. From the curves of Fig. 1, it is felt that the confinement of the dot, for a given number of electrons, is larger for larger top gate bias, so that the confinement potential is changing across Fig. 1.2(a) (in a similar manner to the magnetic field modulated confinement in refs. 7 and 8).

We can extract the capacitance of the top and side-gates to the dot from the above figure. The linearity of the position of the first peak allows us to write $Q = C_g V_g = C_{sg} V_{sg}$, or $C_g = 2.4 C_{sg}$. From the data, we estimate that $C_{sg} \sim 0.7$ aF and $C_g \sim 1.7$ aF. In addition, the dot at the largest negative side gate biases can be extracted from the coulomb gap of Fig. 1.1. For V_g =2.9 V and V_{sg} = –400 mV, $q/2C_{eq}$ = 13 mV, and C_{eq} = 6.2 aF. If it is assumed that the equivalent capacitance is approximately the self-capacitance of a flat disc, $d \sim 15$ nm. Clearly, energy level separation due to confinement can be observed at this dimension.

Finally we consider the addition energy spectrum of the dot at 2.9 V. This is analogous to the affinity in atoms. In Fig. 1.2(b), we plot the voltage V_{sg}–V_{th} for the peaks shown in Fig. 1.2(a). Here, V_{th} is a threshold voltage indicating the onset of coulomb oscillations. We estimate this threshold voltage from the tunneling current curves themselves as the voltage at which tunneling current is seen to begin. However, this is a subjective choice, and thus is somewhat arbitrary. We observe peak splitting as the side-gates are stepped to higher negative voltages. There may even be peak crossings, and there seems to be a splitting of the two "equivalent" valleys for the higher confinements. A particularly interesting structure is the apparent crossing

in the lowest few levels near 3.0 V. We replot these curves for this region in Fig. 1.3, where it may be seen that the second peak has a much larger amplitude than the third for $V_g \leq 3.0$ V and this is reversed for higher top gate biases. Whether or not this is a crossing of the peaks or merely interesting voltage dependent-amplitude variation requires considerably more study. Curves such as this have been used to study Hund's rule in GaAs dots [8], but actually determining an addition energy is not as clear in these Si dots. The valley degeneracy doubles the expected occupancy per degenerate level, and impurities and a tendency of these dots toward non-cylindrical symmetry further complicates the issue.

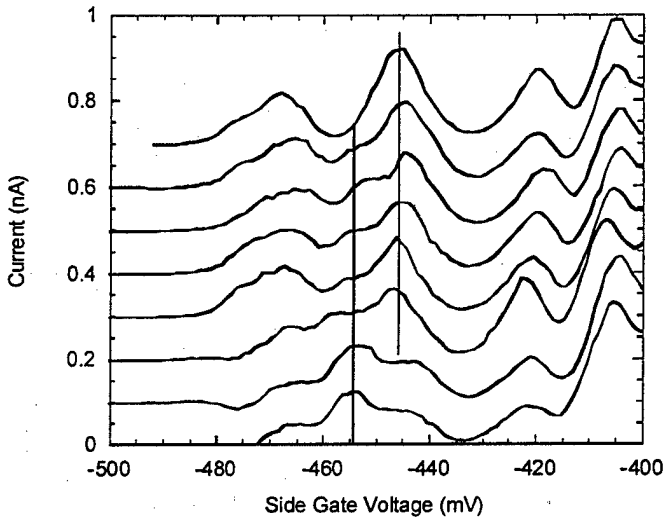

Fig. 1.3 An expanded view of the curves for top gate bias of 2.96-3.1 volt around the initial electron charging region. The lines indicate peaks which may cross, or at least show a shift in line strength.

In conclusion, we have fabricated a silicon quantum dot in a metal-oxide-semiconductor structure. By varying the top gate, we observe movement of the peak in the side-gate characteristic that is reminiscent of experimental observations of a quantum dot in the single electron regime in a magnetic field. In addition, we observe evidence of possible valley splitting normally observed at high magnetic fields and large stresses in silicon inversion layers [9].

1.3 References

1. See, e.g., K. K. Likharev, IBM J. Res. Dev. **32**, 144 (1988).
2. L. Guo, E. Leobandung, L Zhuang, S. Y. Chou, J. Vac. Sci Technol. B **15**, 2840 (1997).
3. L. Zhuang, L. Guo, and S. Y. Chou, Appl. Phys. Lett. 72, 1205 (1998).
4. H. Ishikuro and T. Hiramoto, Appl. Phys. Lett. **71**, 3691 (1997).
5. A. C. Irvine, Z. A. K. Durani, H. Ahmed, and S. Biesemans, Appl. Phys. Lett. **73**, 1113 (1998).
6. M. Khoury, A. Gunther, D. P. Pivin, Jr., M. J. Rack, and D. K. Ferry, Jpn. J. Appl. Phys. **38**, 2083 (1999).
7. M. Rontani F. Rossi, F. Manghi, and E. Molinari, Appl. Phys. Lett. **72**, 957 (1998).
8. S. Tarucha, D. G. Austing, T. Honda, R. J. Van der Hage, and L. P. Kouwenhoven, Phys. Rev. Lett. **36**, 197 (1996).
9. T. Ando, A. B. Fowler, and F. Stern, Rev. Mod. Phys. 54, 437 (1982).

2. Fabrication and Studies of Electron Transport in Coupled Quantum Dots (Prof. J. P. Bird, Arizona State University)

The physical properties of crystalline systems are well understood to be determined by a level hybridization effect, which arises when large numbers of atoms combine to form the crystal structure. According to this effect, the discrete energy levels of the individual atoms are modified due to their incorporation in the lattice, giving rise to the formation of corresponding bands of densely packed crystal states. Such hybridization effects are not restricted to atomic systems, but are expected to crucially determine electron transport through arrays of coupled *quantum dots*, which are small semiconductor devices whose size is comparable to the Fermi wavelength of the electrons themselves [1]. The strong confinement of motion that these dots generate quantizes the electronic energy spectrum into a discrete ladder of states, for which reason the dots are often referred to as *artificial atoms*. When coupled in a multiply connected array, it is therefore expected that the properties of the individual dots will be strongly modified by the emergence of collective, *superlattice*, behavior [2]. In particular, a recent numerical study suggests the possibility of switching successively between insulating and conducting states of such *artificial crystals*, simply by controlling external parameters, such as magnetic field or gate voltage [3]. In any discussion of electron transport through such arrays, it will therefore be imperative to provide a *global* treatment, in which the couplings between individual dots, and their interactions with the external environment, are fully accounted for. Motivated by these considerations, we have undertaken an experimental program of research to fabricate multiply coupled quantum dots and study their transport properties. These structures were realized in high mobility GaAs/AlGaAs heterojunction material using the split-gate technique. Transport studies of the devices reveal the existence of novel localized behavior that is possibly related to the mesoscopic nature of the devices.

2.1 Device Fabrication

The approach we have adopted for fabrication of the coupled quantum dots involves the use of the split-gate technique, in which metal gates with a fine line pattern defined by electron beam lithography are deposited on the surface of a GaAs/AlGaAs heterostructure wafer. With a suitable bias applied to the gates, current flow from source to drain can only occur via the narrow gap between them, whose precise shape is determined by the gate lithography and by the negative bias applied to the gates. An example of a coupled quantum dot structure that we have fabricated using the split-gate technique is shown in Fig. 2.1. This structure allows the realization of two independent dots, whose inter-dot coupling may be tuned directly in experiment. The gates themselves are formed from Ti-Au using standard electron-beam lithography and lift-off techniques. The substrate material consists of high mobility GaAs/AlGaAs heterojunction wafer.

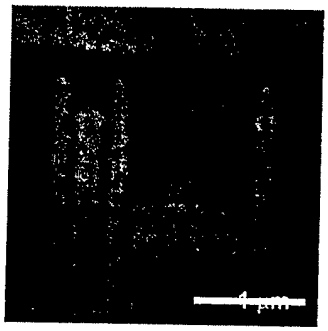

Fig. 2.1. Coupled quantum dot structure realized by the split-gate technique. Darker regions are the high mobility GaAs/AlGaAs heterojunction substrate while the lighter regions are the Ti-Au gates.

2.2 Transport Properties of Coupled Quantum Dots

We have also studied the low temperature transport properties of linear arrays of coupled quantum dots realized by the split-gate technique. These devices reveal novel insulating behavior at low temperatures, according to which the resistance of the arrays increases exponentially as the temperature is reduced. An example of this behavior is shown in Fig. 2.2 below, where the exponential increase is shown for a particular gate voltage setting. Crucially, no evidence for the exponential behavior is observed prior to applying a bias to the gates, indicating that the

localization is associated with the backscattering of electrons induced by the formation of the dot geometry.

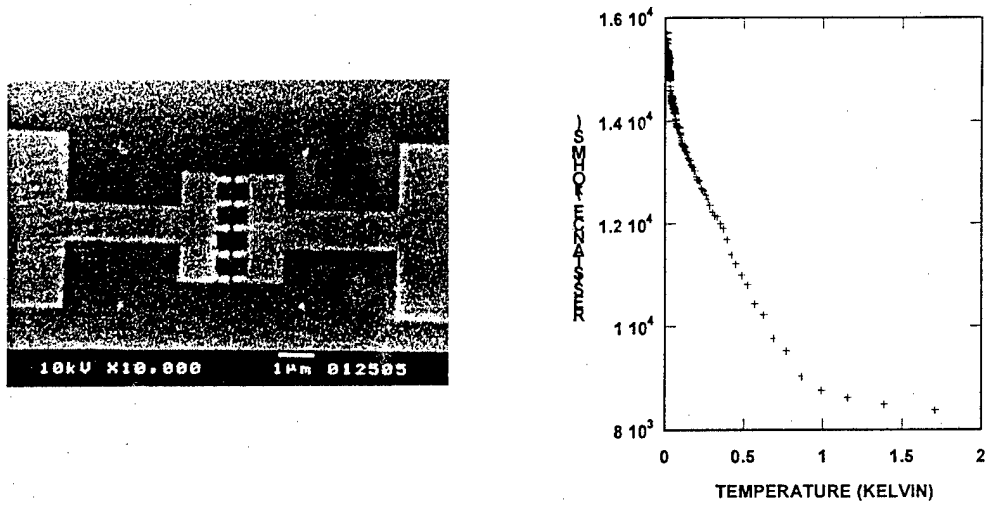

Fig. 2.2. Left: a four-cell linear chain of quantum dots. Lighter regions correspond to Ti-Au gates and the spacer bar denotes 1 µm. Right: measured variation of resistance with temperature in the four-cell linear array.

Unlike the behavior reported in two-dimensional electron systems [4], no evidence for a metal insulator transition is observed in these arrays. The power law exponent of the exponential behavior is also found to be very different to that expected for studies of localization in two-dimensional systems. In this regard, the results of Fig. 2.2 appear to provide evidence for a novel type of localization that is possibly unique to mesoscopic systems. Studies of three different dot arrays have revealed this localization to be strongly device dependent, suggesting that remnant disorder plays a crucial role in its observation. This is not altogether surprising, since the electrical properties of mesoscopic devices are well known to be sensitive to the presence of *individual* impurities. An important and yet unresolved issue concerns the degree of disorder required to generate the localization. Since large variations in behavior are found for devices fabricated on the same wafer, it *may be* that the source of the disorder is simply the donor-induced potential fluctuations that are known to exist in modulation doped heterostructures [5,6]. The results of experiment appear to suggest that the influence of this disorder is further enhanced by the scattering that is generated by the confining walls of the dot. Another interesting feature

of the experiments is the absence of a metal-insulator transition as gate voltage is varied, in either the single dots or the multiply-coupled arrays. We suspect that the absence of any transition may reflect the *reduced dimensionality* of the devices we study. A challenge for future experimental studies is to therefore resolve whether a metal-insulator transition may be observed in these devices.

2.3 Conclusions

We have demonstrated the fabrication of multiply coupled quantum dots and have investigated their transport characteristics. Novel insulating behavior, showing strong sample dependent variations, is found to be generated in the arrays when a gate voltage is applied to form them. This behavior suggests that a proper understanding of electron transport in nanostructure devices will require impurity and boundary scattering to be treated on an equal basis. Future work on these structures should focus on the expected importance of level hybridization effects, analogous to that encountered in molecules, for the transport behavior.

2.4 References

1. *For a review see*: D. K. Ferry and S. M. Goodnick, *Transport in Nanostructures*, Cambridge University Press, Cambridge, UK (1997), and references therein.
2. L. P. Kouwenhoven *et al.*, Phys. Rev. Lett. **65**, 361 (1990).
3. R. Akis and D. K. Ferry, Phys. Rev. B **59**, 7529 (1999).
4. *For a review see*: E. Abrahams, Physica E **3**, 69 (1998).
5. J. A. Nixon and J. H. Davies, Phys. Rev. B **41**, 7929 (1990).
6. M. Stopa, Phys. Rev. B **53**, 9595 (1996).

5. Related Publications

1. M. J. Rack, A. D. Gunther, M. Khoury, D. Vasileska, D. K. Ferry, and M. V. Sidorov, "Compatibility of cobalt and chromium depletion gates with RPECVD gate oxide for silicon based nanostructures," Semiconductor Science and Technology **13**, A71-4 (1998).
2. M. Khoury, A. Gunther, D. P. Pivin, Jr., M. J. Rack, and D. K. Ferry, "A Silicon Quantum Dot in a MOSFET Structure," Japanese Journal of Applied Physics **38**, 469-72 (1999).
3. M. Khoury, M. J. Rack, A. Gunther, and D. K. Ferry, "Spectroscopy of a silicon quantum dot," Applied Physics Letters **74**, 1576-8 (1999).
4. M. Khoury, D. P. Pivin, Jr., M. J. Rack, A. Gunther, and D. K. Ferry, "Fabrication of a Silicon Quantum Dot in a MOS Structure," Nanotechnology, in press.
5. M. D. Khoury, A. Gunther, M. J. Rack, D. P. Pivin, Jr., and D. K. Ferry, "Single Electron Effects in Silicon Quantum Dots in a MOSFET Structure," Microelectronics Journal, in press.
6. J. Allgair, M. Khoury, D. K. Ferry, M. N. Kozicki, and T. K. Whidden, "Nanostructure Grid Fabrication by SEM Exposure of SiO_2," Journal of Vacuum Science and Technology, submitted for publication.
7. Andresen, C. Prasad, F. Ge, L.-H. Lin, N. Aoki, K. Nakao, J. P. Bird, D. K. Ferry, Y. Ochiai, K. Ishibashi, Y. Aoyagi, and T. Sugano, "Localization in an array of quantum dots", Phys. Rev. Lett., *submitted for publication.*
8. Andresen, L.-H. Lin, C. Prasad, F. Ge, N. Aoki, K. Nakao, J. P. Bird, D. K. Ferry, Y. Ochiai, K. Ishibashi, Y. Aoyagi, and T. Sugano, "Insulating state in open quantum dot and quantum dot arrays", to be presented at *Localization 1999*, Hamburg, Germany, July 1999.
9. L.-H. Lin, A. Andresen, F. Ge, N. Aoki, C. Prasad, K. Nakao, J. P. Bird, D. K. Ferry, Y. Ochiai, K. Ishibashi, Y. Aoyagi, and T. Sugano, "Localization and non-equilibrium

electron transport in quantum dot arrays", to be presented at the 11th international conference on *Nonequilibrium Carrier Dynamics in Semiconductors*, Kyoto, Japan, July 1999.

10. L.-H. Lin, A. Andresen, C. Prasad, F. Ge, N. Aoki, K. Nakao, J. P. Bird, D. K. Ferry, Y. Ochiai, K. Ishibashi, Y. Aoyagi, and T. Sugano, "Localization behavior in open quantum dot arrays", to be presented at the 13th international conference on *Electronic Properties of Two-Dimensional Electron Systems*, Ottawa, Canada, August 1999.

3. Single Electron Transistor Neural Nets and Circuit Simulation (Prof. S. M. Goodnick, Arizona State University)

Single-Electron Tunneling (SET) transistors [1] have attractive properties which make them excellent candidates for implementing ultradense and complex signal and image processing systems. SET devices satisfy hardware requirements for large-scale neural networks such as local interconnectivity, small device size and low power consumption. Current fabrication technology allows the integration of 10^{11} SET transistors per cm^2 and a power consumption of 10^9 W per transistor [2]. Ultimately the goal is SET transistors capable of operation at room temperature, and compatible with conventional CMOS process technology. Under the DARPA program, the theoretical capabilities of room temperature SET technology were investigated with the goal of understanding the potential applications, as well as understanding how SET/CMOS circuits could be designed. Various SET circuits were simulated using currently available commercial simulation tools using SET transistors designed to operate at room temperature. In particular, we have investigated SET technology for application to cellular neural networks (CNN) under the DARPA program.

In order for a SET transistor to operate at room temperature, the tunnel capacitance must be on the order of 10^{-19} F. Future reductions of the device dimension are predicted to reach such small capacitances, and hence allow room-temperature operation. Figure 1 shows the simulated I-V characteristics of a SET transistor operating at room temperature. The results were obtained using SIMON1.1, a single electron circuit simulator [3]. A SET inverter circuit [4] consists of two complementary double gate SET transistor of n and p type switches can also operate at room temperature, provided that the capacitance is in the order of 10^{-19} F. Figure 2 shows a modified circuit of Tucker's inverter with its transfer characteristics. While the I-V shown in Fig. 2b does

indeed show inverter-like behavior, the I-V characteristics for more negative and positive bias repeat periodically, which may be problematic for CNN where two stable operating points are traditional required in the cell transfer characteristic.

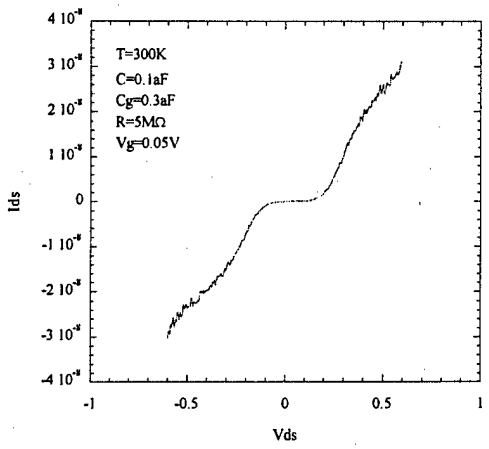

Fig. 1a Drain current of a SET transistor as a function of drain-source voltage.

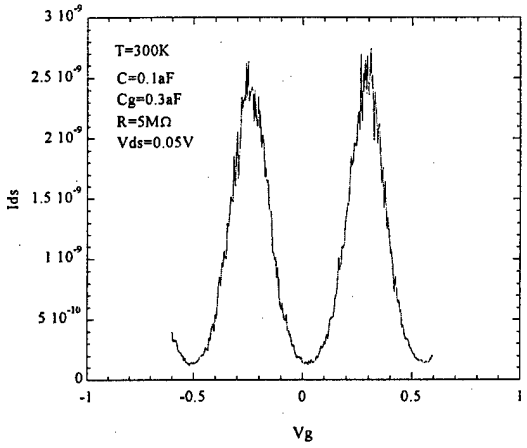

Fig. 1b Drain current as a function of the gate voltage.

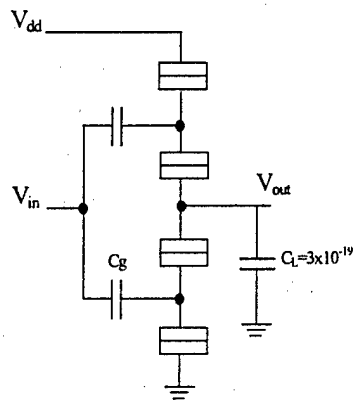

Fig. 2a A modified circuit of Tucker's inverter.

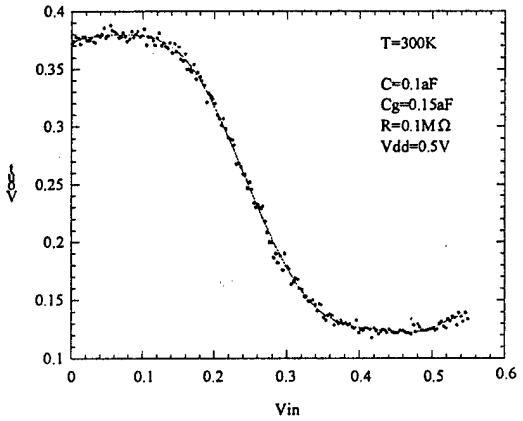

Fig. 2b Inverter output characteristics.

A schematic of an artificial neural network shown in Fig. 3, which consists of a summing node, and a nonlinear activation function which allows for threshold-like behavior in the input-output characteristics. The inverter circuit of Fig. 2 can in fact provide the non-linear activation function using SET technology, provided the node voltage of the summing node does not exceed the range shown there. The summing of the inputs itself can be accomplished by voltage inputs capacitively coupled to the gate of the inverter structure of Fig. 2, as shown by the modified inverter structure with summing capacitor is shown in Fig. 4. There, V_{in} represents one of the multiple inputs, each one capacitively coupled to the same node.

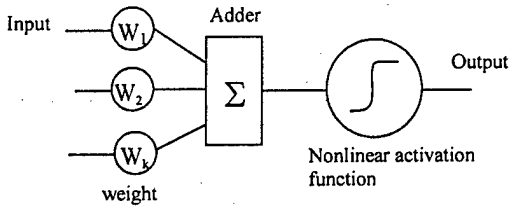

Fig. 3 Neural network model.

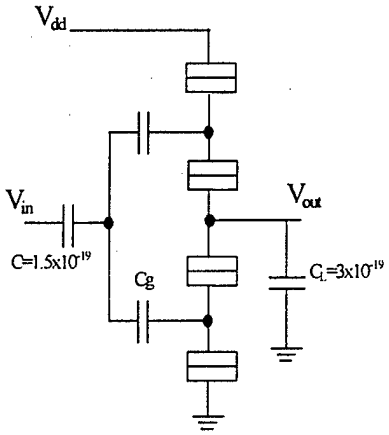

Fig. 4a A modified circuit of Tucker's

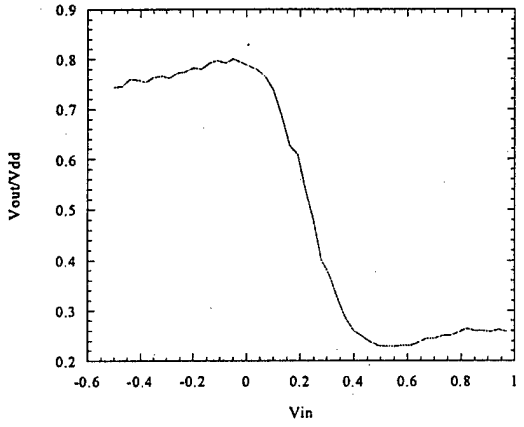

Fig. 4b Circuit output characteristics.

In CMOS technology, the building block of cellular neural networks is the transconductance element (voltage-to-current transducer) that resembles the CMOS inverter [5]. A SET transducer can be realized by connecting two tunnel junctions at the output of the inverter instead of the load capacitor as shown in Fig. 5a. The current I is proportional to the node voltage, hence the transducer I-V characteristic shown in the SIMON simulation of Fig. 5b. Two junctions were found to be necessary at the output rather than a single tunnel junction for stability reasons.

The ability to fabricate the components of cellular neural networks such as summing nodes and transducers is promising for the realization of functional CNNs for massively parallel applications such as image processing. The limitation we have found is the fan out or loading characteristics of the cells circuits shown in Figs. 4 and 5. This may require the outputs of individual cells to be coupled to CMOS buffers which provide the necessary drive between cells, and to the output, which is currently under investigation.

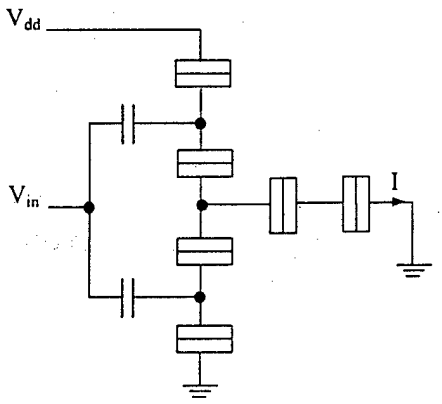

Fig. 5a SET transducer element.

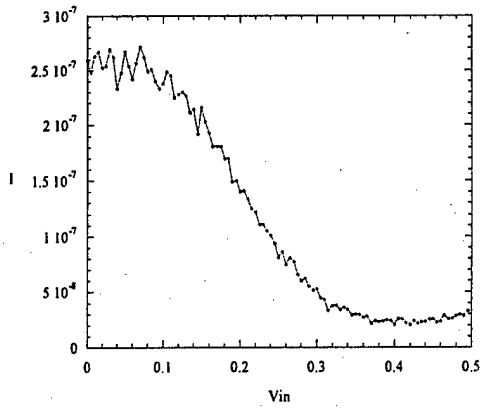

Fig. 5b Transducer output characteristics.

References

1. M.H. Devoret and H. Grabert, Eds., *Single Charge Tunneling, Coulomb Blockade Phenomena in Nanostructures, vol. 294 of NATO ASI Series B:Physics*, Plenum, NY, 1991.
2. R.H. Chen, A.N. Korotkov, and K.K. Likharev, "Single electron transistor logic," *Applied Physics Letters*, 68, no.14, 1954-6, (1996).
3. SIMON (C. Wassshuber and H. Kosina, "A Single-Electron Device and Circuit Simulator", *Superlattices and Microstructures*, 21, 37 (1997).
4. J.R. Tucker, "Complementary Digital Logic Based on the Coulomb Blockade," J. App. Phys. 72, 4399 (1992).
5. I. Baktir and M. Tan, "Analog CMOS implementation of CNN," IEEE Trans. on Circuits and Systems II, 40, no 3, (1993).

4. CEVE Studies (Prof. M. Kozicki, ASU)

There are several reasons why silicon dioxide could be an ideal resist material for ultra high resolution lithographic applications. For example, it forms a hard mask that can withstand harsh processing conditions even in thin film form. This mask can endure dry etching, ion implantation, and even thermal processes far better than any organic material. In addition, the patterned oxide layer may even be left in place as part of a device structure if desired. Selectivity and removal need not be a problem with oxide resists if low density deposited resists, e.g. PVD or spin-cast materials, are used. Thermal oxides could also be utilized in steps which involve the processing of the silicon substrate or polycrystalline silicon layers. A further consideration is that unlike organic resists which contain high molecular weight polymers, amorphous silica has no extended structure at the molecular level. This implies that it may be patterned with an ultimate resolution in the order of a few nm or less.

The desirable properties of SiO_2 in the context of lithography led us to examine processes which may be used to create deep-submicron to nanoscale oxide masks. The process we created and patented, Chemically Enhanced Vapor Etching (CEVE), utilizes hydrocarbon monolayer "sensitizers" which may be crosslinked by electron-beam exposure. The monolayer sensitizers are used in conjunction with HF vapor etching to pattern grown or deposited oxide films to form durable surface masks or device elements.

4.1 Background Work

In recent times there has been considerable interest in vapor phase hydrogen fluoride (HF) etching as a means of both substrate preparation and oxide feature definition [1,2]. Unfortunately, while HF vapor etching of planar substrates is a success, the use of the

methodology to create surface masks at deep submicron or nanoscale dimensions has not been widespread. Our process relies on the fact that vapor-phase HF etching of silicon dioxide will occur if Brønsted bases, including water, are present on the surface of the oxide. To form a masking pattern in an oxide layer using vapor etching, the areas to be removed must have a means of producing or trapping these bases whereas the areas to remain should be free of them. This is possible by having a localized hydrocarbon film as the etch initiator and by keeping the substrate at a temperature which precludes water condensation on the surface of the oxide. In particular, layers of carboxylic acids are capable of both forming and trapping the bifluoride ions necessary for etch initiation. This is the principle of the CEVE technique [3,4].

In our earlier work, we used hydrocarbon contamination layers from laboratory air or vacuum chamber ambients and successfully demonstrated nanoscale pattern formation in SiO_2 [4]. The etch-enhancement regions were fixed by either focussed electron-beam or scanning tunneling microscope (STM) exposure. Such exposures crosslinked the surface hydrocarbons and allowed them to remain after a thermal step which was designed to desorb the uncrosslinked material only. The highest resolution using this technique of around 5 nm was obtained using STM exposure of ambient hydrocarbons on 5 nm thick SiO_2 [5]. Unfortunately, although the attainable resolution can be extremely high, imaging layers formed using hydrocarbons condensed from the ambient are obviously difficult to form reproducibly. Optimum process performance requires the use of molecules that form well-ordered monolayers. For this approach, we chose 10-undecenoic acid, (UA), $H_2C{=}CH(CH_2)_8COOH$, which forms a self-assembled monolayer (SAM) on the oxide surface under appropriate conditions [6]. This carboxylic acid is capable of acting as a Brønsted base and hence will initiate/sustain the etch process in HF vapor when it is in contact with the oxide. It is also capable of being crosslinked by electron-beam exposure, the linkages being formed

between adjacent molecules at the carbon double bond in the backbone. The crosslinked material is used to pattern the substrate after the removal of the unexposed monomer. These monomers adhere well to the surface and so a solvent treatment is used to remove them while leaving the crosslinked material intact. The remaining hydrocarbon pattern is in the order of a few nm in height but is capable of enhancing the etch rate of oxides which are many tens of nm thick [7].

4.2 Summary of Major Results

The first set of results reported here relates to the effect of electron beam exposure of self assembled monolayers of undecylenic acid. Electron beam exposure test patterns, containing boxes and lines with widths ranging from 1 μm down to 20 nm, were used for this purpose. This pattern design allowed for easy feature identification when using the low magnification optical microscope on the AFM system. UA monolayers deposited on SiO_2 were exposed using a focussed electron beam and subsequently immersed in methanol for 5 minutes to remove the unexposed material (solvent treatment is discussed in more detail later). Monolayer formation using room temperature solution immersion was confirmed using Rutherford Backscattering Spectrometry and by ellipsometer [8]. The electron beam dose on all boxes was constant at 700 $\mu C/cm^2$ and linear features were patterned as single-pixel lines, the line dose varying from 1×10^{-8} C/cm to 1×10^{-10}C/cm. The residual patterns in the crosslinked UA were then examined by tapping mode atomic force microscope (TMAFM - Nanoscope IIIa, Digital Instruments, Santa Barbara, California). The TMAFM scans on samples are shown in Fig 1. Fig 1(a) shows the box portion of the pattern. It is clear that despite the width change, the average height of the exposed UA in the boxes is constant at about 1 nm for the constant exposure dose. This value is close to the original thickness of the unexposed undecylenic acid monolayer as measured by

ellipsometer. After the monomers are removed by the solvent treatment, the sample surface in the unexposed regions is essentially bare SiO_2.

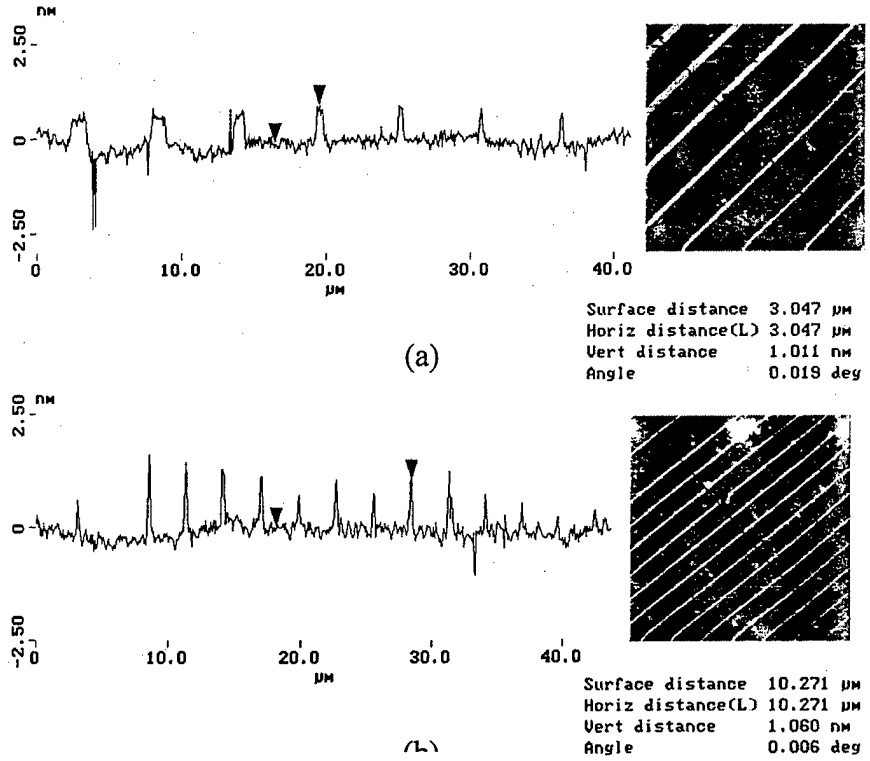

Fig. 1. Tapping mode AFM scans of undecylenic acid self-assembled monolayers on a SiO_2 surface after electron beam irradiation and 5 minutes methanol immersion. All scans were performed in ambient air. (a) The first seven boxes in the test pattern (width decreases from 1μm at upper left to 0.06 μm at lower right). (b) The first thirteen single-pixel lines (electron beam dose varied from 1×10^{-8} C/cm at upper left to 5.4×10^{-10} C/cm at lower right).

Water contact angle measurements on exposed films reveal that the angle on the monolayers decreases as electron beam irradiation increases [9,10]. However, compared to the hydrophilic nature of SiO_2, the SAM regions are still relatively hydrophobic. The UA molecules in the exposed regions are changed structurally and chemically from their monomeric state in the original SAM and these changes result in the observed decrease the original hydrophobicity. This could be problematic as it is believed that water contamination in the AFM measurement

ambient dominates the interaction between the sample and tip, thereby altering the adhesion force [11] and making completely quantitative conclusions difficult. Since a higher hydrophilicity increases the adhesion force, the actual height of the irradiated SAM will be underestimated. However, measurements on the same sample can be used to compare relative feature heights in order to see the effects of exposure parameters. In Fig. 1(b), the change in measured feature height with dose is clear. This TMAFM scan was performed on the line exposures of the test pattern. As the electron beam dose decreases, the apparent height also decreases, suggesting that layer solubility (in methanol) is governed by the irradiation dose. Turning now to Fig. 2, the line with the lowest dose is still visible as a raised line structure. This indicates that during the TMAFM scan on our particular samples, the hydrophilic contrast to SiO_2 will not overcome the actual pattern height for this electron-beam dose range. This figure clearly shows the generally decreasing trend of apparent line height and line width as the dose decreases. We performed careful layer thickness measurements which avoided particles and anomalies and these results are shown in Fig. 3. The apparent height decrease with decreasing electron-beam dose is confirmed and apparently follows a logarithmic relationship. This is to be expected as higher dose will result in more crosslinking which in turn will result in a reduction in solubility. The same effect is evident for all negative-tone organic resists, which exhibit a logarithmically decreasing solubility with exposure dose. Note that Fig. 3 should not be used to derive the contrast of the resist as a wide range in exposed monolayer thickness is capable of producing a high selectivity in the oxide etch (discussed later).

The effect on the SiO_2 etch rate selectivity in HF vapor of immersion of the exposed SAMs in different solvents is shown in Fig. 4 (see [6] for details of the atmospheric pressure etch system and procedures). Solvent immersion is performed immediately after e-beam exposure

and prior to HF vapor etching. The HF vapor etch time was 5 minutes in all cases at a substrate temperature of 110 °C. All samples were etched together. Note that the etch selectivity is defined as

$$SELECTIVITY = \frac{(Etched\ Thickness\ of\ IrradiatedUA\ oxide) - (Control)}{(Etched\ Thickness\ of\ Non-irradiatedUA\ oxide) - (Control)}$$

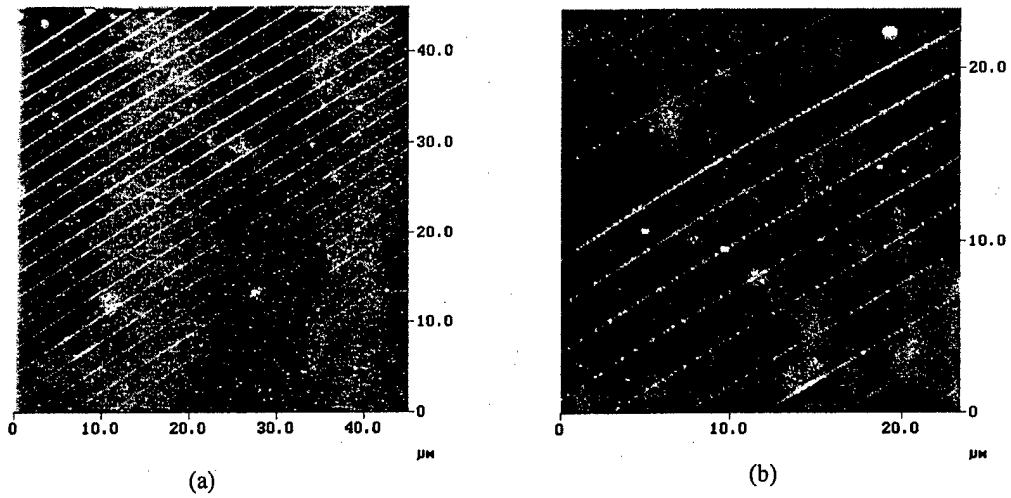

(a) (b)

Fig. 2. (a) TMAFM scans of a large area containing 20 lines. The electron beam dose decreases from upper left corner to lower right corner. The dose range is 1×10^{-8} C/cm to 1×10^{-10} C/cm with a reduction factor of 0.784 between lines. (b) Local enlarged scan. The scanned area is the last two boxes and first seven lines from the upper left of (a).

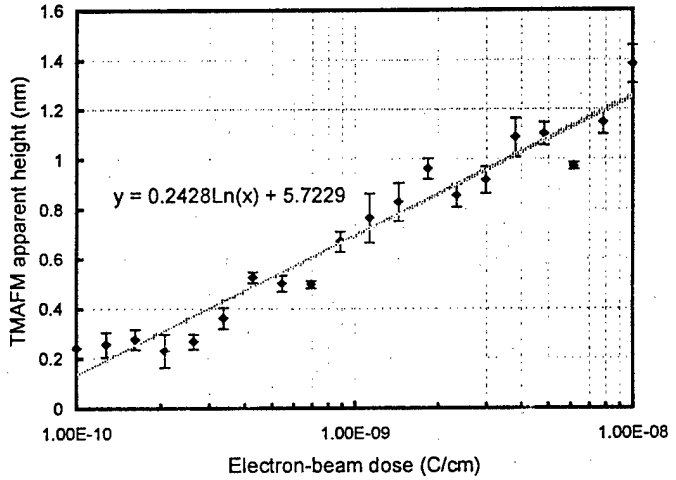

Fig. 3. Apparent height measurement from TMAFM scans. The height is a logarithmic function of electron beam dose.

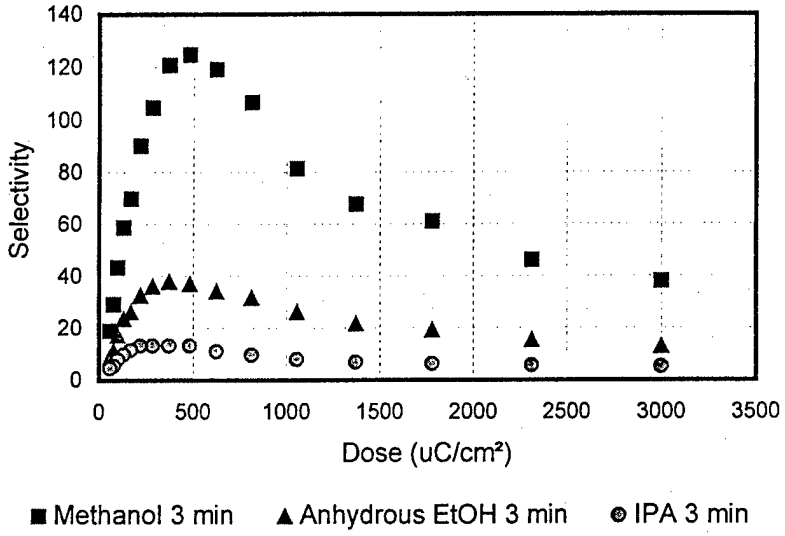

Fig. 4. The effects of immersion in different solvents on the etch selectivity of e-beam exposed UA SAMs on SiO_2.

Clearly, the selectivity rises rapidly with dose in all cases and then decreases at doses in excess of 300 to 500 $\mu C/cm^2$. The highest selectivity of around 125 was obtained using methanol to remove the unexposed monomers while leaving the exposed material intact. The decline in etch selectivity for the highest doses occurs when the exposed post-solvent treated monolayer thickness exceeds 1 nm or so. This is most likely due to the fact that the thicker monolayer actually impedes etchant or etch product transport to/from the surface. This effect is also evident in Figs. 5(a) and (b), which show the effect of dose and electron beam accelerating voltage on etched thickness for thermal oxide and remote plasma chemical vapor deposited oxide respectively. In both cases, the peak selectivity dose increases with increasing accelerating voltage. This is to be expected as a higher electron accelerating energy will result in less energy being deposited at the surface of the film, i.e., there will be less monolayer crosslinking at higher voltage. This will result in a higher solubility during the post-exposure solvent treatment and the resulting film will be thinner and therefore less occlusive.

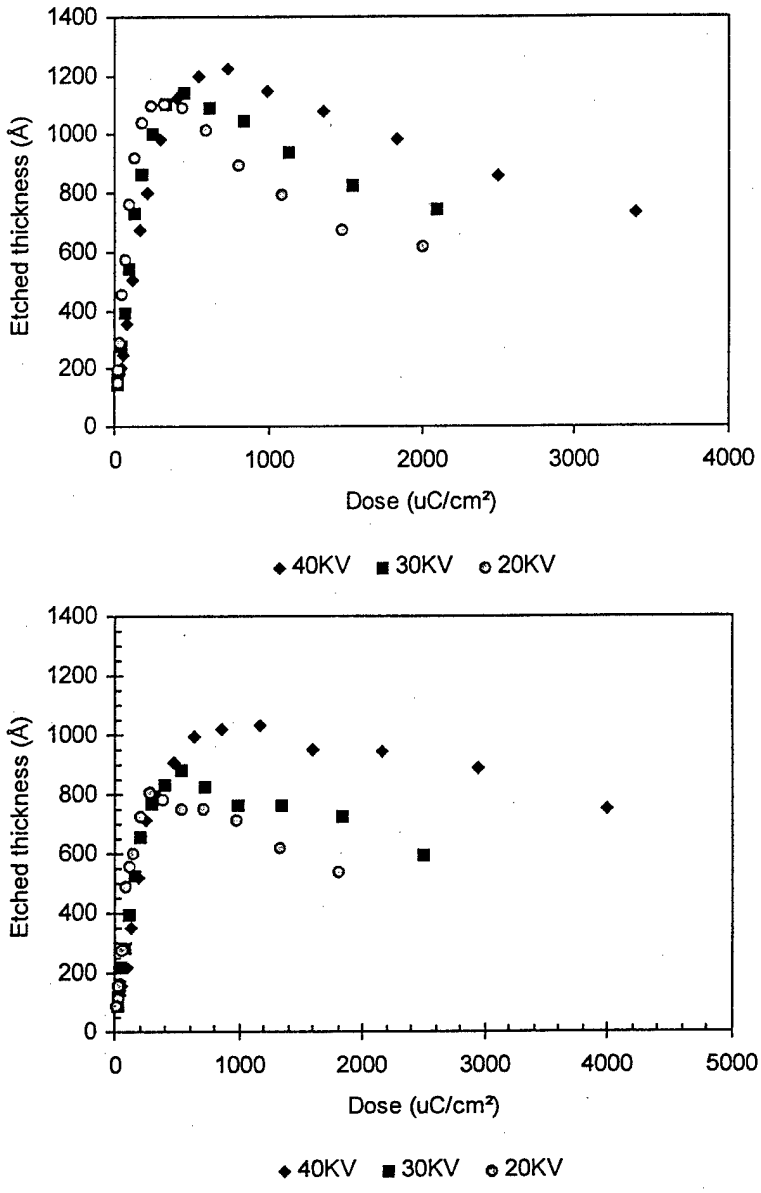

Figure 5. The effect of electron-beam exposure energy and dose on oxide etch rate. (a) Thermal oxide grown at 1050 °C in dry oxygen. (b) Remote plasma CVD oxide deposited at 350 °C from N_2O and SiH_4.

Fig. 6 shows the results of AFM measurements of patterns (trenches) in an oxide film formed by CEVE. These measurements show that although the layer responsible for the etch enhancement is only around 1 nm thick, its ability to "catalyze" and sustain the etch process

leads to features which are in excess of 100 nm deep. This is direct evidence of the fact that the sensitizer layer is not consumed during the etch process and can indeed survive to form deep, anisotropic features in the oxide.

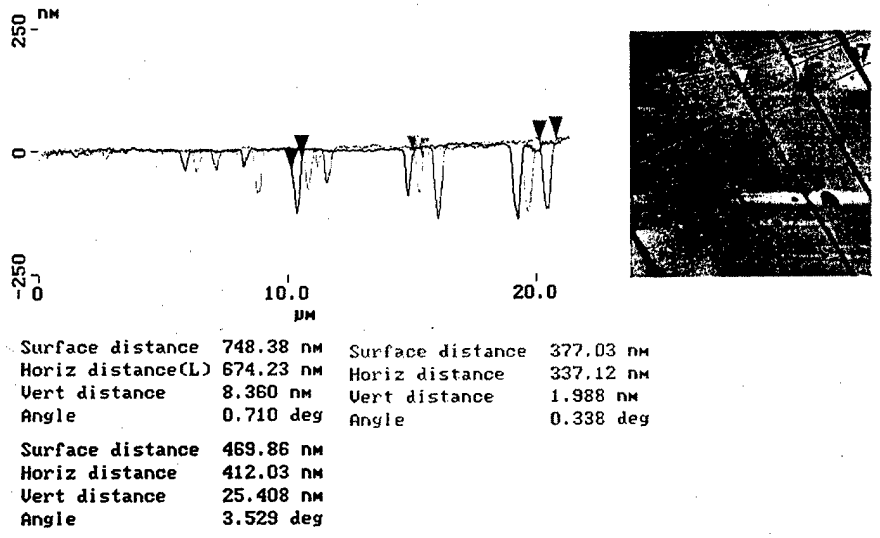

Fig. 6. AFM measurements of trenches in oxide produced by electron-beam exposure of UA, methanol development, and HF vapor etching at 115 °C.

4.3 Cobalt Disilicide Processing

As part of this project we have also formed deep-submicron cobalt disilicide structures by selective metal on silicon reactions [12]. Windows in a thin (10 – 100 nm thick) oxide mask are defined using electron-beam lithography. These windows, which expose the silicon surface, facilitate the localized metal on silicon reactions. The biggest problem with high quality $CoSi_2$ formation is the effect of oxygen in the processing ambient. Even sub-ppm concentrations can result in non-ideal silicide characteristics, especially at small lateral and vertical geometries. To alleviate this problem, we have utilized a thin amorphous silicon layer on top of the Co metal layer as an oxygen scavenger during the silicide formation step. At high ramp rate (>150 °C/s), the reaction for silicide formation is greater than that of Co oxide formation and a high quality

$CoSi_2$ layer forms while the a-Si capping layer scavenges the oxygen by forming a thin silicon dioxide layer on top of the silicide. The oxide is removed by an HF dip after silicidation is complete. Auger electron spectroscopy reveals that the silicide is essentially oxygen-free and the measured resistivities of lines formed using this technique are typically between 19 and 29 μΩ-cm. This compares favorably with the bulk resistivity value of $CoSi_2$ of 18μΩ-cm.

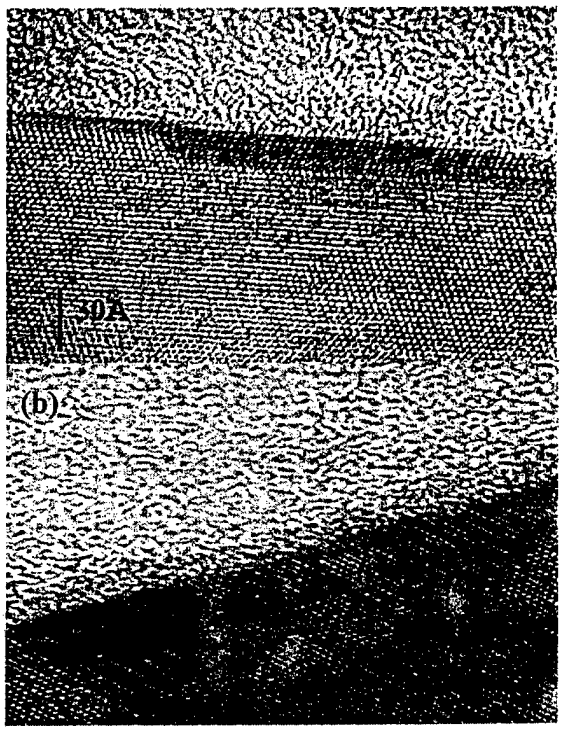

Figure 7. Cross-sectional transmission electron micrographs of ultrathin $CoSi_2$ layers formed on (a) Si (111) and (b) Si (100) substrates.

We have also investigated the formation of ultrathin $CoSi_2$ layers on (111) and (100) substrates using the same formation method. Cross-sectional electron micrographs of silicide formed at 700°C for 20 seconds in an N_2 ambient on Si (111) and (100) substrates are shown in Fig. 7. The initial cobalt thickness was 0.7 nm on the (111) material and 1.0 nm on the (100) silicon. The reaction between Co and Si results in preferential alignment of the $CoSi_2$/Si junction along (111) planes, thus favoring the formation of continuous ultrathin layers of $CoSi_2$ on the Si (111)

substrate, compared with formation of large discontinuous grains of $CoSi_2$ on the (100) substrate. Measurements were performed on macroscopic $CoSi_2$ resistors (10 - 100 μm wide with the separation between the voltage probes between 200 and 1000 μm) formed on Si (111) substrates (resistivity 12 Ω.cm) at 77K to avoid parallel conductance of the Si substrate. As expected, the conductance per square of the film decreased almost linearly with the thickness of the film. The resistivity of the film derived from the data is 7.4×10^{-6} Ω.cm and is about twice as large as the bulk resistivity of the $CoSi_2$ at 77K. Note that the thinnest continuous $CoSi_2$ layers produced on (111) silicon were in the order of 1.5 nm thick.

References

1. P. A. M. van der Heide, M. J. Baan-Hofman and H. J. Ronde, J. Vac. Sci. Technol. A 7, 1719 (1989).
2. M. Wong, M. M. Moslehi and D. W. Reed, J. Electrochem. Soc. 138, 1799 (1991).
3. M.N. Kozicki, U.S. Patent Number 4,904,338 (1989).
4. T.K. Whidden, J. Allgair, J.M. Ryan, M.N. Kozicki and D.K. Ferry, J. Electrochem. Soc. 142, 1199-1205 (1995).
5. T.K. Whidden, J. Allgair, A. Jenkins-Gray and M.N. Kozicki, J. Vac. Sci. Technol. B 13, 1337 (1995).
6. T.K. Whidden, A. Jenkins-Gray, M. Pan, and M.N. Kozicki, J. Electrochem. Soc. 144, 605 (1997).
7. M. N. Kozicki, S.-J. Yang, T. Kim, and B. Kardynal, "A Novel Nanoscale Resist Using 10-undecanoic Acid Monolayers on Silicon Dioxide", to appear in Microelectronic Engineering.

8. T. K. Whidden, S.-J. Yang, A. Jenkins-Gray, M. Pan, and M. N. Kozicki, J. Electrochem. Soc. 144, 605 (1997).

9. K. Seshadri, K. Froyd, A. N. Parikh, D. L. Allara, M. J. Lercel, and H. G. Craighead, J. Phys. Chem. 100, 15900 (1996).

10. B. Völkel, A. Gölzhäuser, H. U. Müller, C. David, and M. Grunze, J. Vac. Sci. Technol. B 15, 2877 (1997).

11. S. J. T. Van Noort, K. O. Van der Werf, B. G. De Grooth, N. F. Van Hulst, and J. Greve, Ultramicroscopy 69, 117(1997).

12. M.N. Kozicki, B. Kardynal, S.-J. Yang, T. Kim, M.V. Sidorov and D.J. Smith, Semicond. Sci. Technol., 13, A63-A66 (1998).

5. **Visualization Software** (Prof. Gerald Farin and Dr. Richard Akis)

We began developing our initial software "vis-a-vis" during the early stages of the project. It was a visualization tool for displaying data that was in the form $z=f(x,y)$. It could handle input data that was on a uniform mesh in the x and y plane and display the third dimension as a color shaded contour plot, a 3D surface plot or a 3D mesh plot. Amongst other things, the interface allowed the user to control the height of the plot as well was the color scheme. One could also rotate the image by using the mouse. One major component was the ability to automatically read in a large number of consecutively numbered data files and assemble them into short animated sequences, lasting 10 seconds or so. The animated sequences (of changing mesh or surface patterns) were of significant importance in the detection of phenomena that would not be visible in static images. The program could then output the resulting images individually as JPEG files, or save the entire animated sequence as an MPEG movie file. This software was mainly developed by E. Shafer.

In its second version, we eventually enhanced "vis-a-vis" by adding visual aids such as coordinate axes boxes, and cross-sectional slices. An example of this is shown in the left panel below. This shows the full visavis graphical user interface, the interior of which displays a 3D surface plot of a quantum dot potential enclosed by an axes box and intersected by two cross-sectional slices. The positions of these slices is controlled by the mouse. Note that the interface incorporates pull down menus and slide bars that control the various other program options. The program was also modified to allow input data that was on a non-uniform mesh. This is illustrated by the right panel, which shows a 3D mesh plot of this same quantum dot potential. We also incorporated a variety of additional graphics formats for the images to be saved in, such as GIF and Postscript. These additions were mostly carried out by S. Rahman.

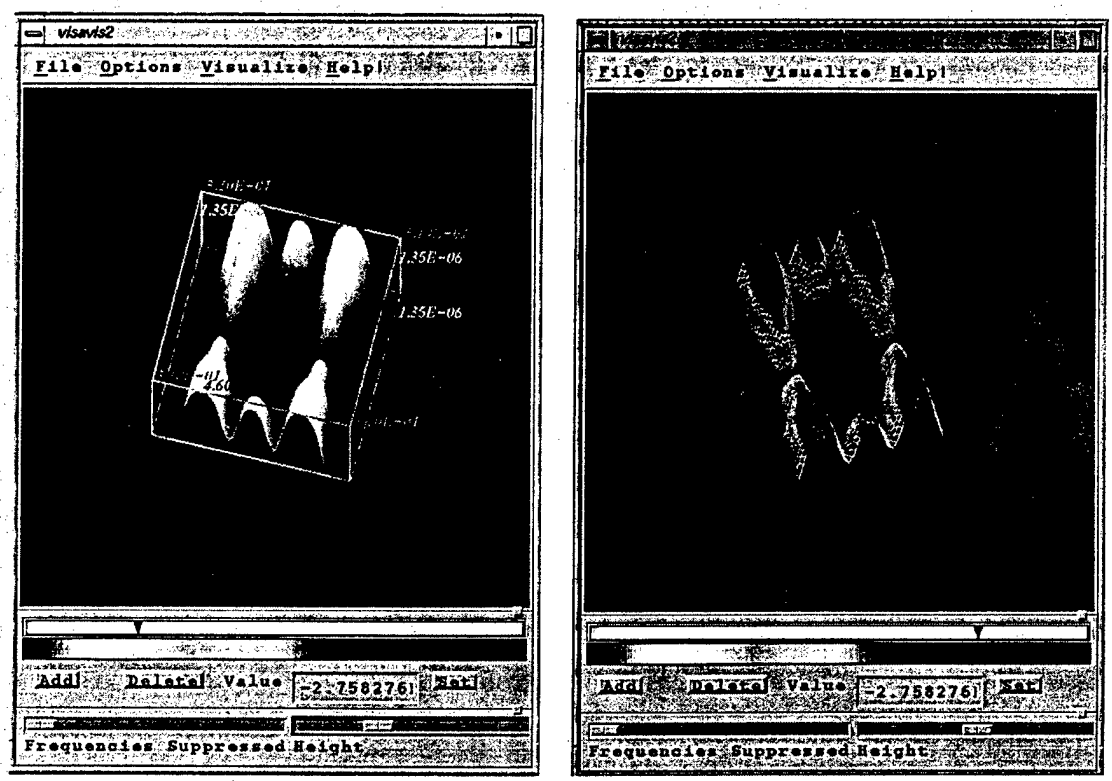

Fig. 5.1 Vis-à-vis panel for softare simulation.

6. Transport Theory (H. L. Grubin, SRA, Inc.)

6.1 Dissipation as a Precursor to Device-Device Interaction

One of the issues addressed during the course of this study was an appropriate formulation of dissipation, as well as its implementation. Dissipation is an essential ingredient for studying device-device interactions. Broad guidance as to what should be incorporated in the analysis can be gleaned from studies of classical systems, but this can only take us so far. To begin, the classical equation of transport, the Boltzmann equation without dissipation (and ignoring time dependence) is $k\partial f/\partial x+(\partial V/\partial x)\partial f/\partial k=0$. This has the generic solution: $f(x,k)=g\left(k^2/2-V(x)\right)$ which is symmetric with respect to momentum and consequently yields zero current. With transients the time dependent distribution function symmetry with respect to momentum and a finite time-dependent current occurs.

But a primary device issue is the correct prediction of steady d.c. current for which the dissipationless Boltzmann equation is inadequate. A simple relaxation-time approximation, $k\partial f/\partial x+(\partial V/\partial x)\partial f/\partial k+f/\tau=0$, is often invoked that removes the symmetry with respect to momentum, yielding a finite d.c. current: For a constant field, a solution is $f(x,k)=g\left(k^2/2-V(x)\right)exp-\left[k/\tau F\right]$, where g is an arbitrary function determined by initial conditions. This solution, in general, does not lead to Ohm's Law. Incorporating an equilibrium distribution and dealing with fields small enough to be consistent with linear response theory does indeed yield Ohm's Law. Incorporating time dependence as well as an equilibrium distribution results in the generic solution (for a constant field):

$$f(x,k)=-exp\left[\frac{k}{\tau F}\right]\int_0^k dk'\left(\frac{f_0(k')}{\tau F}exp\left[-\frac{k'}{\tau F}\right]\right)+exp\left[\frac{k}{\tau F}\right]G\left(\frac{k^2}{2}+Fx,k+Ft\right)$$

Here $G(\Phi,\Omega)$ is an arbitrary function determined by boundary and initial conditions. Traveling along a characteristic direction leads to the standard Chamber-Rees solution to the transport problem. In which case depending upon the assumptions made Ohm's law can be retrieved.

Regardless of how much detail is included in classical transport studies, the essential theoretical issue is the representation of scattering (which is more general than the simple relaxation time) and the subsequent solution of the transport equation. The quantum mechanical situation is richer, as we discuss below, but the primary nature of dissipation is unchanged. Since dissipation is essential for a steady current flow, why are most conceptual models based solely upon ballistic transport? Furthermore, how is ballistic transport treated, if dissipation must be dealt with in device discussions? The response to both questions is straightforward: *The study of ballistic transport as an isolated event without regard to dissipation is wrong! With regard to the second issue, ballistic transport and dissipation can be treated as non-isolated events.* The latter is known from early studies of vacuum tube physics where information about electrons is obtained after they dissipate their energy (and/or momentum) at the anode.

The fact that knowledge of transport is acquired subsequent to dissipation, and additionally, that measurement influences the properties of quantum states indicates that transport is best dealt with numerically. And when dealing with quantum devices in which the barrier/well regions are treated ballistically, the surrounding dissipative regions must be incorporated into the device study on an equal footing. Rarely has this been done. For example the literature is filled with simulations in which the device is typically 50 or 60 nanometers while the quantum mechanical barrier region is typically 15 nanometers long. Most of the regions surrounding the active region, particularly in the vicinity of the boundaries display density profiles that are non-uniform, and thus do not properly represent the presence of contacts which

are incorporated solely to provide the necessary role of dissipation. (Active contact regions of the type known from transferred electron device operation are ignored here.) Experience has indicated that the region surrounding the quantum mechanical region should be at least 50 to 100 nanometers long to properly deal with the cladding regions.

We have done much better with classical device simulations. One need only take a look at the use of simulation tools to design state-of-the-art transistors used in most Intel processors to recognize this fact. Indeed, the level of confidence needed to design quantum structures is low, due in part to inability of these algorithms to simulate what is ostensibly a simple problem: Ohm's Law. Presently, the highly approximate quantum hydrodynamic equations and the quantum Liouville equation in the coordinate representation are the only simulations that appear to be able to simulate Ohm's Law.

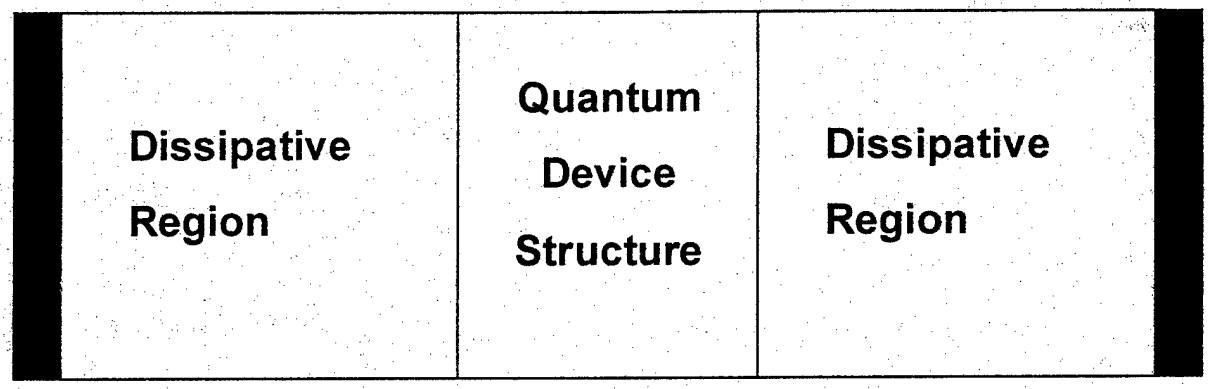

Fig. 6.1 Schematic of a quantum structure and its surrounding dissipative regions.

Classical algorithms do well because of the incorporation of dissipation in the basic models. The simplest manifestation of dissipation in classical models is through the mobility model in the semiconductor drift and diffusion equation. But more generally when dealing with either the moments of the Boltzmann transport equation or directly with the Boltzmann equation dissipation is often dealt with through *boundary conditions!* For example in the case of the

Boltzmann transport equation asymmetry in the current carrying states can be introduced at the boundaries through the use of a displaced Fermi distribution if we were certain that this was a suitable representation of the boundary.

But the use of boundary conditions to deal with dissipation avoids the critical device issues, as addressed below, and represented schematically as shown in Fig. 6.1 (as discussed recently by Ferry and Barker [1]). The nature of transport in the dissipation regions must be addressed with the same degree of sincerity as transport in the ballistic region. The apparent simplicity of Fig. 6.1 belies the nature of the difficulty of treating dissipation properly without including the relevant phase space coordinates. For example, in its simplest manifestation, the one space dimension has at a minimum, at least one additional momentum direction. And it is the conditions associated with the momentum direction that define the role of dissipation.

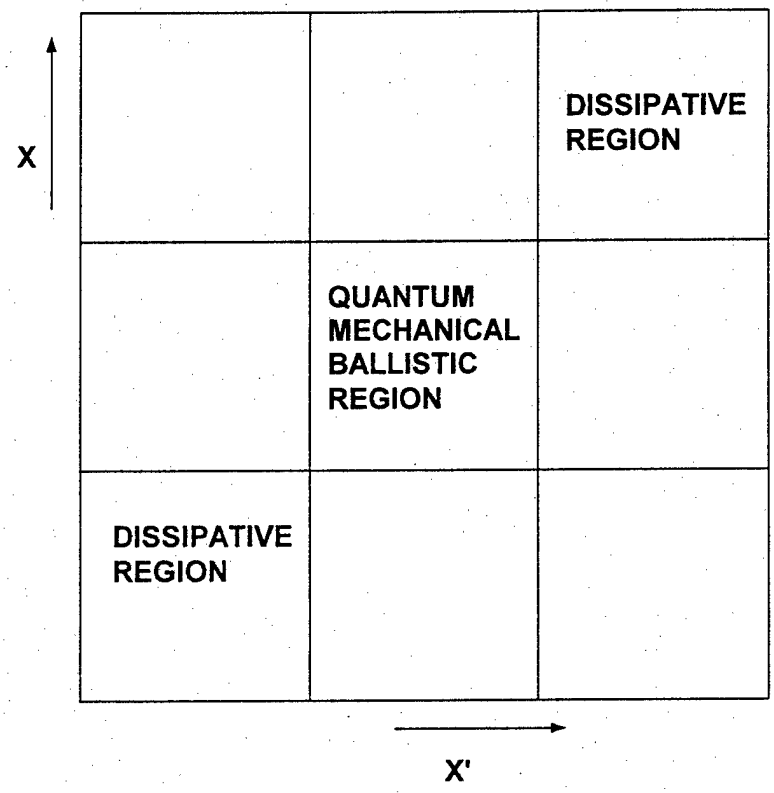

Fig. 6.2. Coordinate phase space representation of a device and its associated dissipative regions

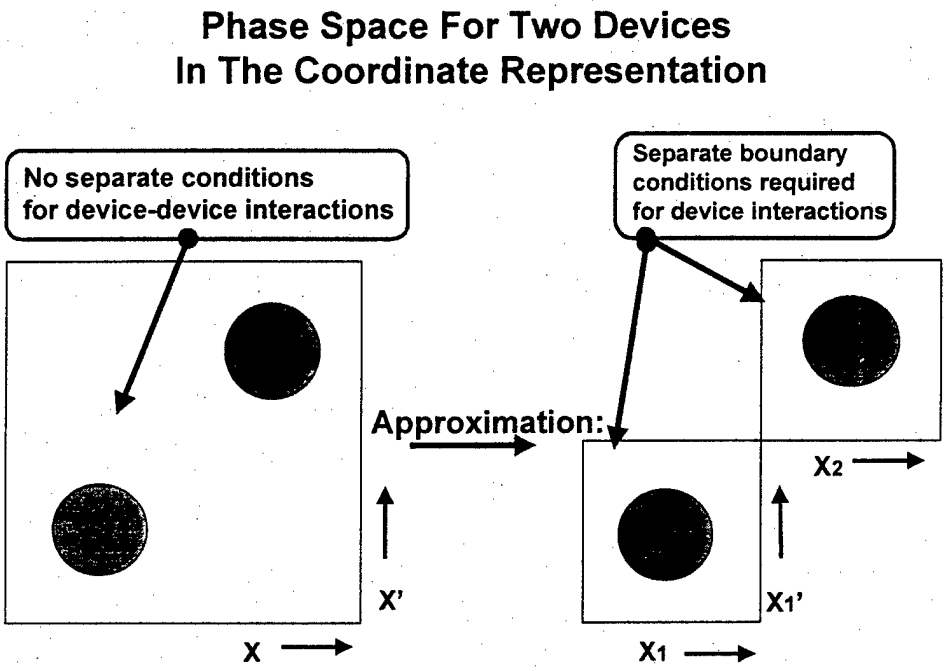

Fig. 6.3. Schematic of device-device interaction within a complete and approximate coordinate phase-space representation.

Perhaps a more relevant diagram that argues for treating dissipation on the same level as ballistic transport is one that represents the formulation of the above problem within the framework of the quantum Liouville equation in the coordinate representation as shown in Fig. 6.2. Solving the equation of motion of the density matrix in the coordinate representation involves specifying conditions on two orthonormal axes, in this case the x and x' axes--note that one-dimensional device concepts are usually pictured along the diagonal $x = x'$. Thus as in the one-dimensional Fig. 6.1 structure, Fig. 6.2 consists of the device region surrounded by dissipative regions. But here, boundary conditions are established at regions that are removed from the actual device. These boundaries indicate the presence of correlation effects, and are present whether the device and its surroundings are represented in the coordinate phase-space picture or the momentum-coordinate phase-space picture. The issue of treating dissipation is present when studying device-device interaction, where there is an exchange of energy between

the devices; and this is what we want to deal with. Figure 6.3 is a schematic representation of the treatment of device-device interaction. The shaded circles represent the device and consist of all of the regions represented by Fig. 6.2. Clearly, the most direct way of dealing with device-device transport issues is to solve the relevant quantum transport equations for the entire structure, as represent by the left hand diagram of Fig. 6.3. Given the limited computational resources presently available, most will opt for a second approach, which is to treat the influence of one device on the next as an alteration in the boundary condition, see right hand panel. How is this done?

Suppose we had two interacting quantum mechanical devices and that they were sufficiently removed from each other that the interaction took place via alterations in the net potential difference seen by each device. In this case, each device is an isolated device and device-device interaction becomes a device-circuit problem. On the other hand, if the devices were close enough so that the influence of one was strong enough to alter the boundary conditions typically seen by the other, then the result will be a distorted charge distribution, which in turn will alter the dynamical behavior of the structure studied. We examined this problem within the framework of the density matrix in the coordinate representation.

Figure 6.4 is a representation of a device with a specification of values of the density matrix along one of the boundaries. Derivative boundaries are also imposed, or some combination thereof, for a complete specification of the problem. The boundary condition: $\rho_{boundary} = exp - \left[(x - x')^2 / 4\lambda^2 + \beta V((x + x')/2) \right]$ is suitable for a classical region with a potential energy $V(r)$ without any interaction with any other devices. To represent the influence of other devices on this boundary, we distorted the potential distribution on the

boundary and examined its influence on the charge distribution. The potential distribution was distorted by shifting the value of the potential on the boundary.

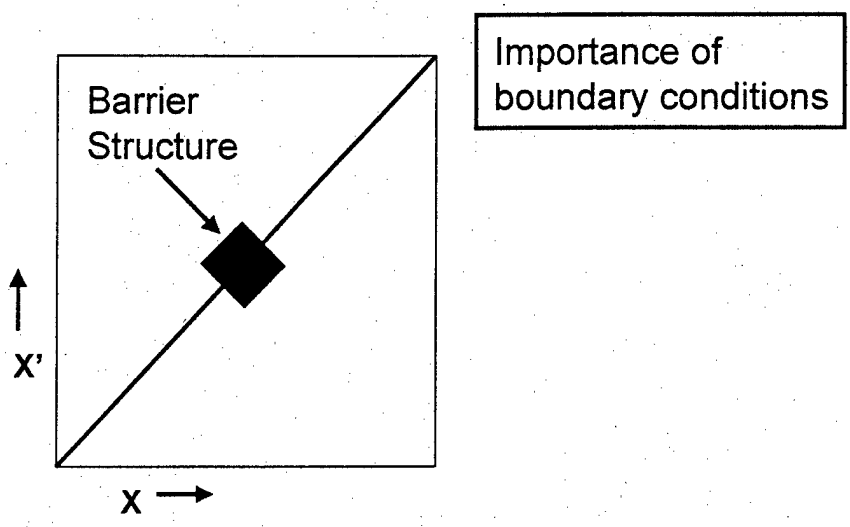

Fig. 6.4. Schematic of a quantum structure with part of the imposed boundary condition.

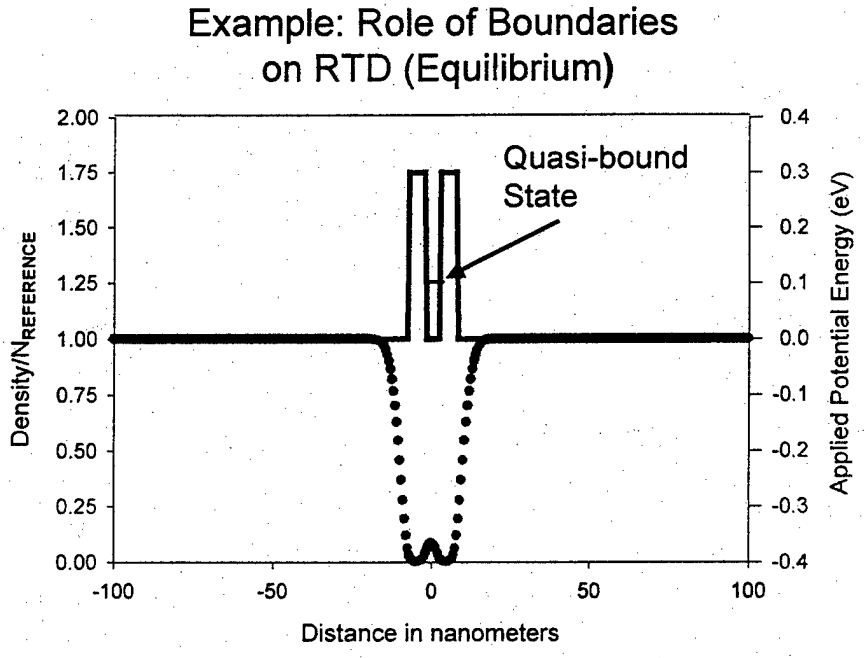

Fig. 6.5. Non-self consistent equilibrium solution to the quantum Liouville equation in the coordinate representation.

For reference, Fig.e6. 5, displays a non-self consistent calculation using the quantum Liouville equation in the coordinate representation under equilibrium conditions. The non-

equilibrium situation is displayed in Fig. 6.6, where we show the effects of distorting the boundary. There is, of course the build-up of charge in the quantum well. For modest changes in the potential energy there is a modest distortion of the charge distribution, but for larger distortions the charge is displaced, a result that will have dramatic effects on device performance. As far as the scale is concerned, it appears that these effects become more pronounced as the device structure decreases in size. Devices whose scale is of the order of up to ten thermal deBroglie wavelengths will be profoundly affected by variations in the boundary conditions and thereby the influence of other devices.

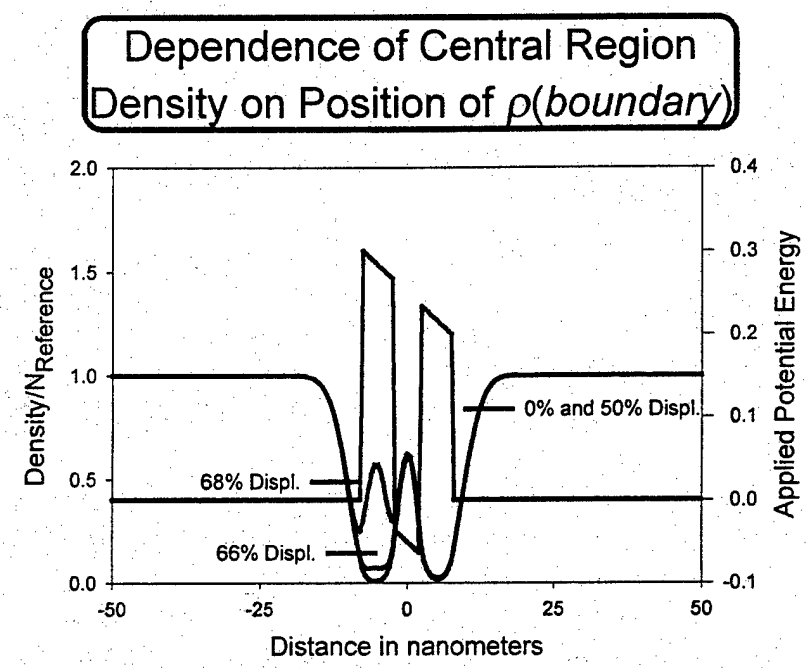

Fig. 6.6. The effect of distorting the boundary condtion on the non-equilibrium charge distribution with a quantum structure.

6.2 The Quantum Device Equations

What were the device equations used in this study? We dealt with two types of equations in performing simulations of device transport. We also dealt with a generic form of transport to derive a general expression for dissipation. The first equation for which most of the studies was

performed was the quantum Liouville equation in the coordinate representation. The quantum Liouville equation in the coordinate representation including a contribution from dissipation can be written as:

$$i\hbar\left(\frac{\partial\rho(x,x',t)}{\partial t}+\left[\frac{\partial\rho(x,x',t)}{\partial t}\right]_{Dissipation}\right)$$
$$=-\frac{\hbar^2}{2m}\left(\frac{\partial^2\rho(x,x',t)}{\partial x^2}-\frac{\partial^2\rho(x,x',t)}{\partial x'^2}\right)+V(x,x')\rho(x,x',t) \tag{6.1}$$

$$V(x,x')\equiv V(x,t)-V(x',t) \tag{6.2}$$

If we introduce a phenomenological relaxation time:

$$\left[\frac{\partial\rho(x,x',t)}{\partial t}\right]_{Dissipation}\equiv\frac{\rho(x,x',t)}{\tau} \tag{6.3}$$

For a constant relaxation time, the quantum Liouville equation is Hermitian. If we consider only dc steady state transport, the resulting transport equation is complex. Where does this dissipation come from? Recently Ferry and Barker [1] discussed the existence of a complex potential energy as a primary source of dissipation. This would clearly fit within the framework of the single particle density matrix, and would yield a Hermitian density matrix if the complex potential had the following special properties: property:

$$\phi(x,x',t)\equiv V(x,x't)+i\theta(x,x',t)$$
$$\theta(x,x',t)=\theta(x',x,t) \tag{6.4}$$

This complex potential is more complicated than that arising from a one-dimensional optical potential, commonly used in the Schrödinger equation. The question of course is: should we seek a density matrix in the present of dissipation that is Hermitian? The introduction of Fokker-Planck dissipation into the formulation does not alter the Hermiticity of an already Hermitian equation.

The situation when dealing with the single particle Wigner function requires the same care when dealing with dissipation. For example in the absence of dissipation, this equation is:

$$\frac{\partial f(x,k,t)}{\partial t}+k\frac{\partial f(x,k,t)}{\partial x} + \int_{k_0}^{k_0} dk'\left(\int_{L}^{+L} dy\left(V(x+y)-V(x-y)\right)exp\left[2i(k-k')y\right]\right)f(x,k',t)=0 \tag{6.5}$$

Under time-independent steady-state conditions, the above equation is symmetric with respect to momentum and does not generate any finite current unless current is assumed to flow via the boundary conditions. The presence of a scattering term would as in the case of the classical Boltzmann equation yield current flow.

While the above discussion points to some critical omissions in the discussion of transport, it only begins to address the consequences of scattering and dissipation in quantum system. Nanoscale dimensions and terahertz frequencies introduce a significant number of other contributions, as summarized below.

6.3 Dissipation Formulation for Nanoscale Devices

What is the basis of the above dissipation considerations? This is considered below for systems that are out of equilibrium. In the following, we find it necessary to distinguish between the system providing all of the device issues and the reservoir. We will formally designate the system we are studying by the letter ***S***. The letter ***R*** will denote the reservoir. The system ***S*** is exchanging energy with other systems and is therefore not in a state of equilibrium. For the moment we ignore all references to specific representations [e.g., equation (6.3) was expressed within the framework of the coordinate representation, whereas equation (6.5) is within the framework of a Wigner representation]. The quantum Liouville equation for the total system, ***S*** plus ***R*** is:

$$i\hbar\frac{\partial \rho_T}{\partial t} = [H, \rho_T] \equiv \hat{H}\rho_T \tag{6.6}$$

Here the 'carat' over the operator, designates a super-operator, as reviewed in Ref. [2]. The super-operator here, also called the Liouville operator, is a commutator-generating super-operator, whose use simplifies the algebra associated with separating the reservoir and system.

The density operator that yields the quantum Liouville equation in the coordinate representation, equation (1), is the reduced density operator. The reduced operator is obtained by averaging over the reservoir coordinate contributions; i.e. by taking the trace over the eigenstates of the reservoir, $\rho_S = Tr^{(R)}\rho_T$, (with a similar definition for the reduced density operator for the reservoir, $\rho_R = Tr^{(S)}\rho_T$).

With H_S, H_R, and H_{SR} denoting, respectively, the Hamiltonian of ***S***, ***R***, and the interaction, between the reservoir and the system of interest the Liouville equations for the reduced density operators $\rho_S = Tr^{(R)}\rho_T$ and $\rho_R = Tr^{(S)}\rho_T$ are, respectively:

$$i\hbar\frac{\partial \rho_S}{\partial t} = [H_S, \rho_S] + Tr^{(R)}[H_{SR}, \rho_T], \tag{6.7}$$

$$i\hbar\frac{\partial \rho_R}{\partial t} = [H_R, \rho_R] + Tr^{(S)}[H_{SR}, \rho_T]. \tag{6.8}$$

The presence, in equations (6.7) and (6.8), of $Tr^{(S)}[H_{SR}, \rho_T]$, or the total density operator, means we do not have a prescription for obtaining an equation for the reduced density operator. All of the effort below is devoted to dealing with this issue.

Our approach, which is based upon the work of Haken [3], allows for a general decomposition of the system and reservoir even when they are significantly *entangled,* as is often the case for far-from-equilibrium situations.

6.4 Projection Operators and the Time Dependent Liouville Equation

From equation (6.6) we consider the projection operator, P, and its complement Q, where $P+Q=1$. The operator P is chosen so that $P\rho_T = RTr^{(R)}\rho_T = R\rho_S$, $Tr^{(R)}R=1$, $PR=R$. The operator R is chosen to represent the uncoupled distribution of the reservoir, e.g., $R \to f_R = exp[-\beta H_R]/Tr^{(R)}\{exp[-\beta H_R]\}$. Thus, the effect of the operator P is to take the density (or other) operator, *average over all the non-equilibrium coordinates of the reservoir*, and generate a density operator that is a product of the *equilibrium* reservoir operator and the reduced density operator of the system [4]. *The effect of the reservoir is still present in the density operator of the system, but its effect has been smoothed over.* The dimension of the subsequent operator is the same as that of ρ_T. It is easy to demonstrate that $P^2=P$, and that P is a proper projection operator. Then, starting from equation (6.6), and after some super-operator algebra, the time dependent Liouville equation becomes for the reduced system operator becomes (we have also assumed that at $t=0$, when the interaction is initiated, the density operator is separable into orthogonal operators for the system and the reservoir.):

$$i\hbar\frac{\partial\rho_S}{\partial t} = \hat{H}_S\rho_S + \hat{\tilde{H}}_{RS}\rho_S - \frac{i}{\hbar}Tr^{(R)}\hat{H}_{RS}(t)\int_0^t d\tau U(t,\tau)\hat{H}_{RS}(\tau)R\rho_S(\tau)$$

$$+\frac{i}{\hbar}Tr^{(R)}\hat{H}_{RS}(t)\int_0^t d\tau\left(PU(t,\tau)\hat{H}_{RS}(\tau)R\rho_S(\tau)\right) \qquad (6.9)$$

$$+\frac{1}{\hbar^2}Tr^{(R)}\hat{H}_{RS}(t)\int_0^t d\tau\left(Q\int_t^\tau d\tau' U(t,\tau')P\hat{H}(\tau')V(\tau',\tau)\hat{H}_{RS}(\tau)R\rho_S(\tau)\right)$$

Here,

$$\tilde{H}_{RS} = Tr^{(R)}(H_{RS}R)$$
$$V(t,\tau) = exp-\frac{i}{\hbar}\int_{\tau} d\tau' \hat{H}(\tau')Q \quad . \tag{6.10}$$
$$U(t,\tau) = exp-\frac{i}{\hbar}\int_{\tau} d\tau' \hat{H}(\tau')$$

Let us take a look at equation (6.9). The first term on the right-hand-side represents the standard system Hamiltonian operator. The second term represents a non-dissipative modification of the system. The illustration of Fig. 6.4 is an example of this contribution. Additionally, a quantum dot with coupling through quantum point contact is another example, as discussed later. The third term is a new non-perturbative term. It is first order in the reservoir coordinates, incorporates dissipation and the intra-collisional field effect contributions. The intra-collisional field effect, for example, arises from the presence of the total Hamiltonian in the exponential of the operator $U(t,\tau)$. The fourth term is also new. It is second order in the reservoir coordinates and at least second order in the interaction Hamiltonian. The last term is an expansion to all remaining orders of the reservoir coordinates and can provide validation of present perturbation theory! The last three terms on the right-hand side of equation (6.9) represent the effect of *scattering* by the fluctuations in the reservoir. These terms all contribute to an equivalent *self-energy*.

The above discussion detailed the separation of the system and reservoir coordinates from an operator viewpoint and yields an operator equation in which the reservoir is introduced as a perturbation. But all of the operator variables are in terms of system coordinates. Let us digress for a moment and look at the problem from the point of view of the wave functions and then the density matrix in the coordinate representation. Figure 6.7 is a representation of a density matrix coordinate system that is diagonal along the '*q*' direction.

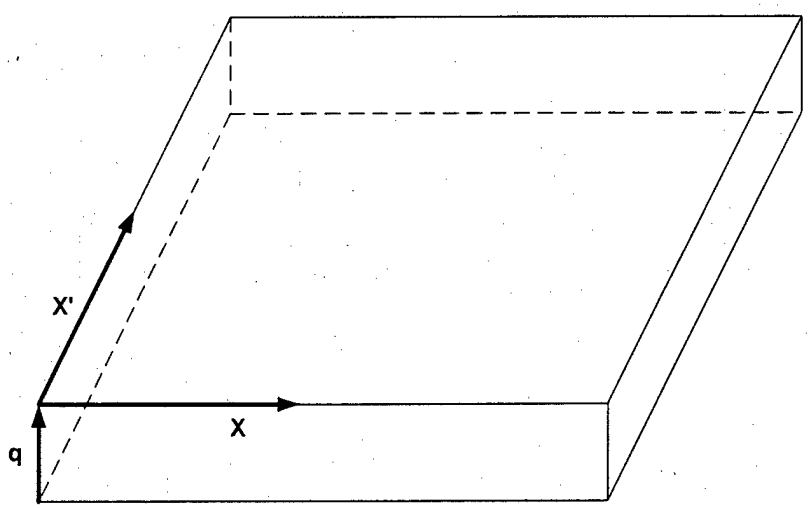

Fig. 6.7. Representation of a coordinate system for a four-dimensional density matrix that is diagonal along the 'q' direction.

If $\Psi(x,q,t)$ represents the time-dependent wave function of an electron and phonon state, then the density matrix, which is constructed from these wave functions is represented as $\rho(x,x';q,q')$. The phase space we need to deal with is four-dimensional. For simplicity let us consider a situation that is diagonal in the reservoir coordinates, in which case we deal with the density matrix $\rho(x,x',q)$. The computational zone is shown in Fig. 6.8.

Figure 6.8 is more general than anything we have dealt with in the past, as it involves an explicit coordinate for dissipation. In the past we have dealt with the density matrix within a two dimensional framework and treated the effects of dissipation through a perturbation analysis as described earlier. But if we view the device-reservoir in terms of Fig. 6.8, then we can imagine that the role of dissipation, which certainly affects the distribution of charge, would influence this distribution differently for different device designs. Indeed variations in device design, in addition to dissipation will influence the shape of the electron distribution. We illustrate this for two cases one with strong coupling to a reservoir, and a second with weak reservoir coupling.

(a) (b)

Fig. 6.8. Plot of the diagonal elements of the density matrix, i.e., the square of the magnitude of the wave function, for a square quantum dot subject to different reservoir couplings. (a) The coupling is through tunneling barriers; (b) the coupling is via conducting wave-guides supporting two modes. The nature of the coupling creates differences in the density matrix for the system.

We consider a square quantum dot, in the presence of a magnetic field and concentrate on the diagonal terms of the density matrix in the coordinate representation, $\rho_S(x,y;x,y) = \mid \Psi(x,y) \mid^2$. The square quantum dot is coupled to the reservoirs through point contacts (these are observable in Fig. 6.8(a)). Here, with the point contacts opened, entering particles form a collimated beam, which excites a particular set of eigenstates and reproduces semi-classical orbits [5]. The excitation is not limited to a single eigenstate, but excites a specific set of modes [6]. In contrast if the quantum point contacts are closed down (Fig. 6.8(b)) to create tunneling barriers (the weak coupling limit), then the properties are quite uniform across the dot. If we vary an applied magnetic field, the transmission function exhibits a series of sharp tunneling peaks. It is clear that, by comparing Fig. 6.8(a) and Fig. 6.8(b), the actual values of ρ_S are dramatically affected by the specific details of the interaction with the reservoir. The above analysis is predicated on separating the system and reservoir coordinates. What if, instead of dealing with the interaction of the device with the reservoir we dealt with device-

device interaction? Here, many, but not all, of the approximations leading to equation (6.9) would remain intact. In particular, one key approximation that would be discarded is that associated with the equilibrium of the reservoir. we see that we can parameterize the interaction in terms of an equilibrium coordinate.

Another important point is that the energy level shifts and coupling that occur by opening the system to the reservoir are distinctly different from the scattering properties, which lead to level broadening. The former arise from the second term on the right of equation (6.4), while the latter arises from the last three terms on the right of equation (6.4). Scattering from the reservoir can either cause broadening of the levels, or actually work to stabilize the regular orbits [7]. It might be expected that the latter case would actually lead to narrowing of discrete energy levels.

More generally, what is done with equation (6.9) depends upon the problem of interest. For the case where the term H_{RS} is linear in the momentum [8], the dissipation may be expressed in terms of a quasi-Fermi energy model [9]. Ahn [10] treated the reservoir as stochastic, performed a time average on equation (6.4), and obtained a quantum kinetic equation for interacting electron and hole pairs. Krech *et al.* [11] developed a master equation to study macroscopic quantum tunneling of charge in ultra-small single electron tunneling double junctions.

We shall consider some of the more general features of this equation. The third term, which was obtained without the use of perturbation theory, includes the intra-collisional field effect. If the off-diagonal elements of the density operator in the momentum representation are taken as small compared to the diagonal elements, we obtain the quantum kinetic equation discussed by Ferry [2], as well as that of Kreiger and Iafrate [12]. This third term incorporates energy conservation, but only within the system ***S***. We note that the results of Ref. [12] were

obtained through perturbation theory with the interaction Hamiltonian as the perturbation estimate. The results here are not totally dependent upon approximations, and suggest a broader applicability of the results of Ref. [12]. Higher-order terms corresponding to the detailed role of the reservoir are readily accessible. These will be discussed in more detail elsewhere.

6.5 Green's Functions

We also implemented Green's functions methods to examine the role of boundaries and structure on device behavior. The emphasis was on structure and how simple structural variations manifest themselves in changes, sometimes dramatic, in the conductance versus energy relation. The simplest structural variations include the *effects* of isolated impurities on the output of quantum point contacts, and in the case of open quantum dots the effects of placement and opening width on the conductance. In the latter case we find that structural variations can change conductance versus energy relations from the familiar plateau structure to one where the conductance displays oscillations. This study is limited in scope to rectangular structures of finite potential energy. The soft potential arising from self-consistency is not treated, and we expect the appearance of some oscillations, while not spurious in a mathematical sense, would not appear experimentally.

We note that the recursive construction of Green's functions on a tight-binding lattice is not new. As used below, a damping factor, $i\eta$, is included. Each of the examples discussed below involves the Kubo formalism for computing the conductance. For this study we specify the potential energy distribution and compute the conductance for a specific Fermi energy. To set the stage for the results we refer to Fig. 6.9 for a structure in which the point contact opening on the left is smaller than that of the right. First some details. The structure is defined on a 30x60 equally spaced rectangular array. The lattice spacing is 5nm. The width of this structure

is W=145nm, the widths W1=W2=50nm, W3=W4=20nm, the lengths L=295, L1=95nm, and L2=100nm. For this structure the potential energy on all of the boundaries as well as the shaded region were set at $6V_{aa}$, where $V_{aa} = \frac{\hbar^2}{2ma^2}$. For a=5nm and m the effective mass of GaAs electrons V=24.2meV.

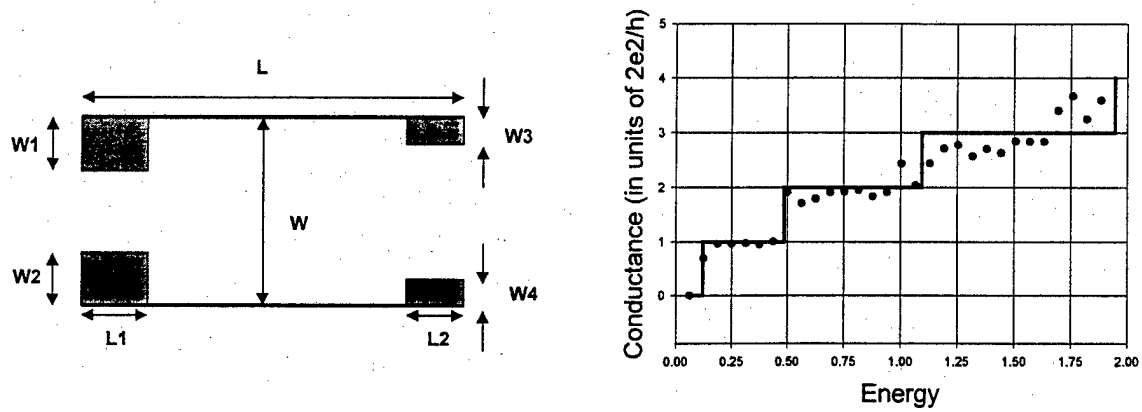

Fig. 6.9. Conductance versus normalized Fermi energy for the structure in the inset.

The points in the right panel of Fig. 6.9 display the conductance as a function of Fermi energy. The solid lines in the figure are obtained from the ideal conductance; $G = \frac{2e^2}{h}\frac{k_f W}{\pi}$, where the number of modes is given by: $M \approx \frac{k_f W}{\pi} = \frac{W}{a\pi}\sqrt{\frac{E_F}{V_{aa}}}$, and W is the opening of the left most point contact. The results are clearing dominated by the quantum point contact with the smaller opening, a result that appears to be consistent with earlier discussions. (Note, in this formula we see an equivalence where the number of modes increases as the gate bias is made less negative, and increasing the number of modes by increasing the Fermi energy through an increase in the numbers of carriers.) The calculations take a strong turn, with the appearance of oscillations, when the opening of the second quantum point contact is reduced to that of the first

one, see Fig. 6.10. These results remain qualitatively the same for structures in which the separation of the quantum point contacts is increased to 2 microns. The solid line is Fig. 6.10 is the same as in Fig. 6.9. It is apparent that the magnitude of the conductance would be better fitted if reduced by a factor of '2', where the inverse of the conductance are additive.

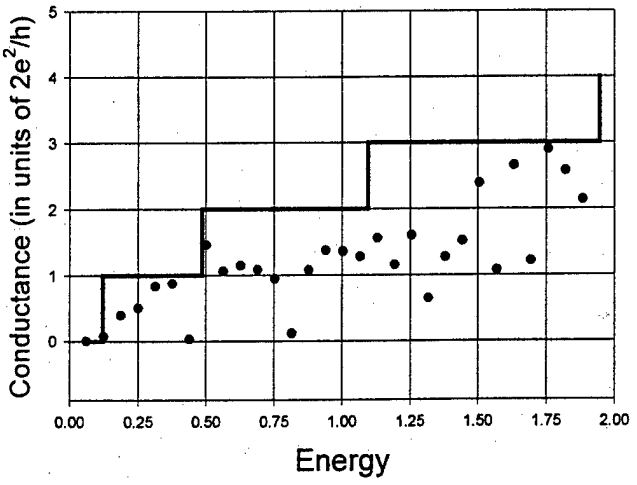

Fig. 6.10. Conductance versus normalized Fermi energy for the structure in the inset.

It is expected that the conductance variations are dependent upon geometry. In addition to the above structures, the conductance was computed for the structures shown in Fig. 6.11. Figure 6.11(a) showed conductance variations similar to that of Fig. 6.9. Figure 6.11(b), which is another representation of an open quantum dot, displayed a more regular set of conductance plateaus, suggesting the importance of geometry in the interpretation of conductance behavior. Calculations with Figs. 6.11(c) and 6.11(d) were performed to determine the role of such things as isolated impurities on the conductance. The situation for Fig. 6.11(c) resulted in only marginal changed in the conductance from a 'perfect' point contact, while that for Fig. 6.11(d), where the change is over a longer distance, resulted in severe distortions. Some of the latter are probably consequences of the sharpness of the boundaries.

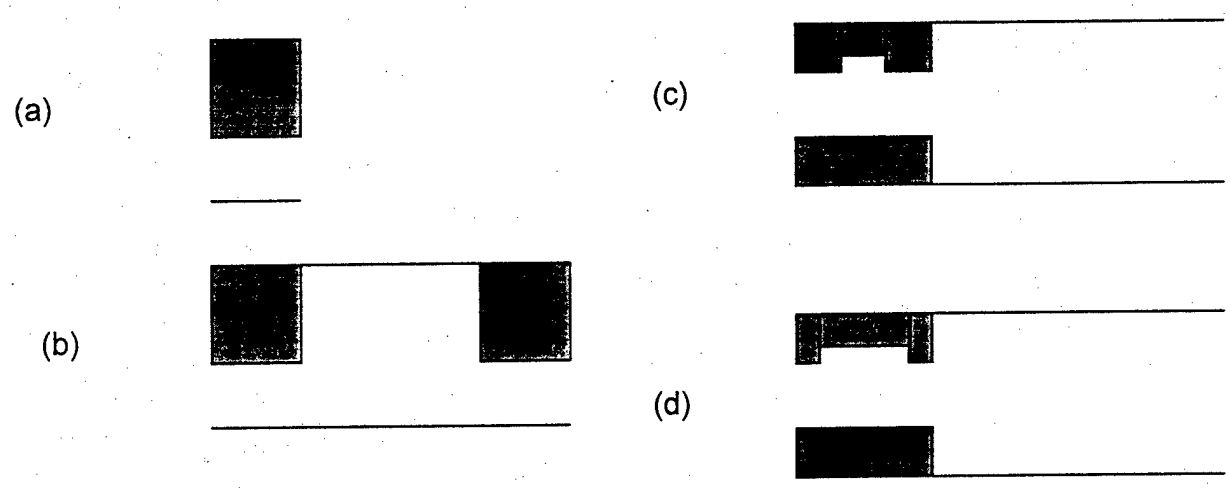

Fig. 6.11. Various structures studied

This Greens function study was undertaken to demonstrate how simple structural variations manifested themselves in changes, sometimes dramatic, in the conductance versus energy relation. The studied demonstrated the *effects* of isolated impurities on the output of quantum point contacts, and in the case of open quantum dots the effects of placement and opening width on the conductance. In particular, we found that structural variations can change conductance versus energy relations from the familiar plateau structure to one where the conductance displays oscillations.

References

1. D. K. Ferry and J. R. Barker, Appl. Phys. Letts **74,** 582 (1999)
2. D. K. Ferry, *Semiconductors* (Macmillan Publishing Company, NY, 1991).
3. H. Haken. *Rev. Mod. Phys.* **47**, 67 (1975)
4. A similar approach has been used to project a many-particle distribution onto an effective one-electron distribution function by J. Zimmermann, P. Lugli, and D. K. Ferry, *Sol. State Electron.* **26**, 233 (1983).
5. R. Akis, D. K. Ferry and J. P. Bird, *Superlatt. Microstructure,* in press.
6. L. A. Wu, *Phys. Rev.* **A53**, 2053 (1996).

7. B. S. Helmkamp and D. A. Browne, *Phys. Rev. Lett.* **76,** 3691 (1996).
8. I. R. Senitzky, *Phys. Rev.* **119**, 670 (1960)
9. H. L. Grubin, T. R. Govindan and D. K. Ferry, *Proc. Ninth Hot Carriers in Semiconductors* (to be published.)
10. D. Ahn, *Phys Rev.* **B50,** 8310 (1994).
11. W. Krech, A. Hadicke, and F. Seume, *Phys. Rev.* **B48** , 5230 (1993)
12. J. B. Krieger and G. J. Iafrate, *Phys. Rev* **B35**, 9644 (1987).

7. **Process Simulations** (H. L. Grubin, SRA, Inc.)

We also embarked on a program to perform silicon based nanostructure process modeling at the equipment level. We did this: (1) to understand process mechanisms as a complement to experiment, and (2) to enhance process design, optimization and subsequent process control (important manufacturing issues). Two types of models are necessary for this task:

1. Equipment level models (developed at SRA), and
2. Wafer / feature level models (developed at ASU).

On the equipment level model the requirements include the

1. Model input includes complete reactor geometry including inlet, outlet, wafer size, location, etc.
    a. Heating / cooling of walls / wafer
    b. Plasma: Power coupling (RF, ICP, ECR)
    c. Parameters with "knobs" for control of
        i. Flow rates
        ii. Pressure
        iii. Plasma Power
        iv. Plasma: Additional wafer bias.
2. Model data base includes:
    a. Transport properties
    b. Thermochemical properties
        i. Gas phase
    c. Reaction kinetics
        i. Gas phase

ii. Surface

3. Model output includes:

   a. Gas flow patterns

   b. Gas temperature profiles

   c. Neutral species distributionAt the wafer: species concentration and flux, temperature.As indicated in Fig. 7.1 below, SRA provides input for the region within the circle.

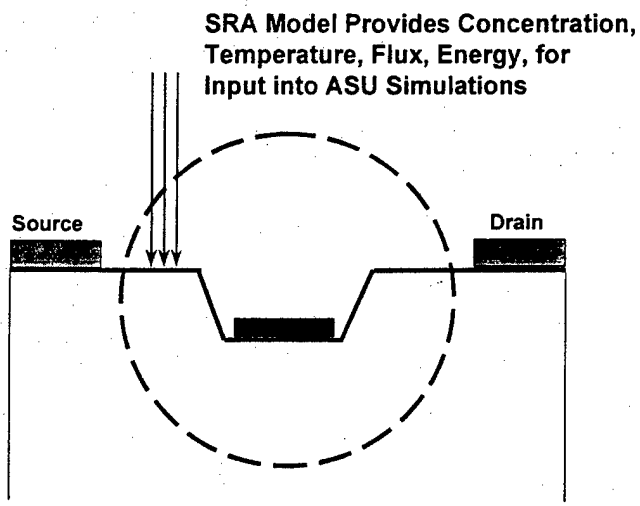

Fig. 7.1. Schematic of input for process modeling.

The output is growth / etch rate, profile evolution, final feature shape and stoichiometry. These results are compared with data from ASU. The studies that were performed included that of the following reactor configuration, Fig. 7.2, in which we were concerned about the electron density distribution. In this case we were interested in the electron distribution in the simulation region displayed in Fig. 7.3. The results are displayed in Fig. 7.4.

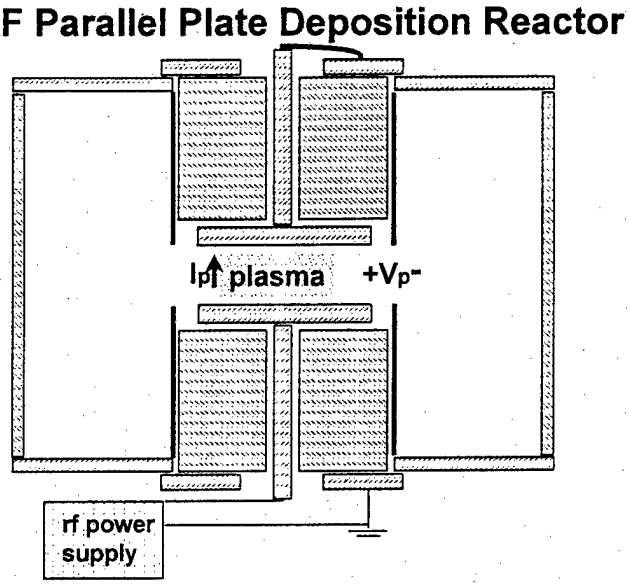

Fig. 7.2. Reactor design used in simulation

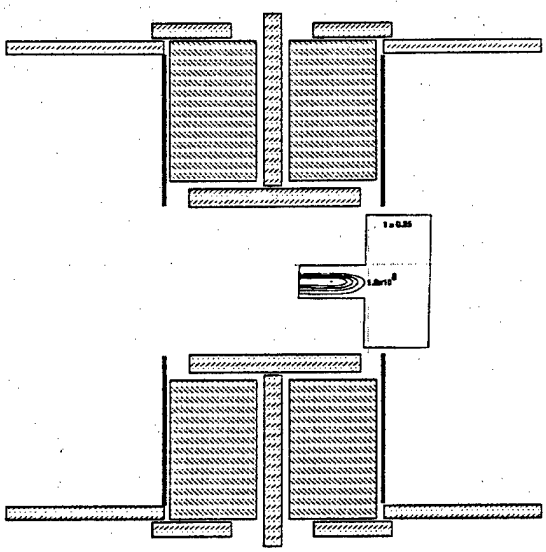

Fig. 7.3. Simulation region.

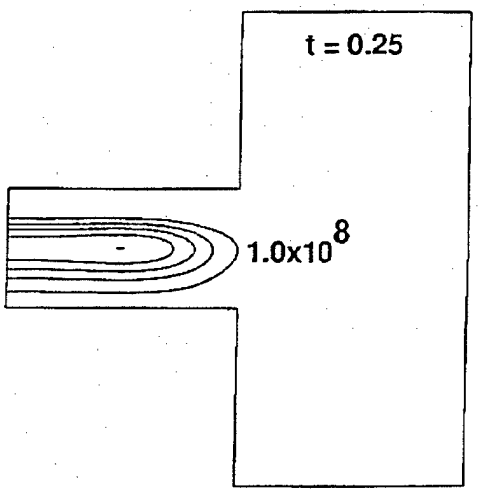

Fig. 7.4. Electron density contours for the reactor of Fig. 7.3.

8. Publications

1. R. Akis, D. K. Ferry, and J. P. Bird, "Numerical simulations of quantum dots: Quasi-periodic conductance fluctuations, scarred eigenfunctions, and the breakdown of the semi-classical transport," Superlattices and Microstructures **20**, 323-30 (1996).
2. R. Akis, J. P. Bird, and D. K. Ferry, "The effects of inelastic scattering in open quantum dots: Reduction of conductance fluctuations and disruption of wave-function 'scarring'," Journal of Physics Condensed Matter **8**, L667-L674 (1996).
3. R. Akis, D. K. Ferry, and J. P. Bird, "Magnetotransport Fluctuations in 'Regular' Semiconductor Ballistic Quantum Dots," Physical Review B **54**, 17705-15 (1996).
4. R. Akis, D. K. Ferry, and J. P. Bird, "Wave-function scarring effects in stadium-shaped quantum dots," Physical Review Letters **79**, 123-7 (1997).
5. R. Akis, J. P. Bird, and D. K. Ferry, "Wave function scarring in open ballistic quantum dots," Japanese Journal of Applied Physics **36**, 3981-5 (1997).
6. R. Akis and D. K. Ferry, "The role of periodic orbits in the magnetotransport of coupled, open, ballistic dots," Solid-State Electronics **42**, 1297-1301 (1998).
7. R. Akis and D. K. Ferry, "Wave function scarring effects in Sinai billiard cavities," Physica B **249-251**, 355-363 (1998).
8. R. Akis, D. Vasileska, D. K. Ferry, Y. Okubo, Y. Ochiai, J. P. Bird, K. Ishibashi, Y. Aoyagi, and T. Sugano, "Stability of regular orbits in ballistic quantum dots," Physica B **249-251**, 368-372 (1998).
9. R. Akis and D. K. Ferry, "Closed versus open: To what extent to the leads influence the magneto-transport in square quantum dots?" Semiconductor Science and Technology **13**, A18-20 (1998).

10. R. Akis and D. K. Ferry, "Wave-function scarring effects in open ballistic quantum cavities," VLSI Design **8**, 307-12 (1998).

11. R. Akis and D. K. Ferry, "Ballistic Transport and Scarring Effects in Coupled Quantum Dots," Physical Review B **59**, 7529-36 (1999).

12. R. Akis, D. Vasileska, D. K. Ferry, and J. P. Bird, "Zero Field Magnetoresistance Peaks in Open Quantum Dots: Weak Localization or a Fundamental Property?" Journal of Physics: Condensed Matter **11**, 4657-64 (1999).

13. R. Akis, J. P. Bird, D. K. Ferry, and D. Vasileska, "Nonuniform energy level broadening in open quantum dots: The influence of the closed dot eigenstates on transport," Physica E, in press.

14. J. Allgair, T. K. Whidden, M. N. Kozicki, and D. K. Ferry, "Formation of Nanoscale Cobalt Silicide and Gold Wires Using E-Beam and Chemically Enhanced Vapor Etching (CEVE)," Journal of Vacuum Science and Technology A **14**, 1855-9 (1996).

15. J. Allgair, J. M. Ryan, H. J. Song, M. N. Kozicki, T. K. Whidden, and D. K. Ferry, "Nanoscale Patterning of Silicon Dioxide Thin Films by Catalyzed HF Vapor Etching," Nanotechnology **7**, 351-5 (1996).

16. J. P. Bird, A. P. Micolich, H. Linke, D. K. Ferry, R. Akis, Y. Ochiai, Y. Aoyagi, and T. Sugano, "Environmental coupling and phase breaking in open quantum dots," Journal of Physics Condensed Matter **10**, L55-61 (1998).

17. J. P. Bird, R. Akis, D. K. Ferry, D. Vasileska, J. Cooper, Y. Aoyagi, and T. Sugano, "Lead Orientation Dependent Wavefunction Scarring in Open Quantum Dots," Physical Review Letters **82**, 4691-4 (1999).

18. G. Edwards, A. Grincwajg, and D. K. Ferry, "Simulations of Fluctuations in Quantum Wire Mesoscopic Systems," Japanese Journal of Applied Physics **34**, 4348-52 (1995).

19. G. Edwards, A. Grincwajg, and D. K. Ferry, "Calculations of Magneto-Transport Fluctuations in Ballistic Quantum Dots," Surface Science **361/362**, 714-7 (1996).

20. G. Edwards, A. Grincwajg, and D. K. Ferry, "Classical and Wave-Mechanical Aspects of Magneto-transport Fluctuations in Ballistic Quantum Dots," Physica B **227**, 144-7 (1996).

21. G. Edwards and D. K. Ferry, "Lattice Effects in the Complex Subband Dispersion of 2DEG Semiconductor Waveguide Structures Subjected to a Perpendicular Magnetic Field," VLSI Design **6**, 31-4 (1998).

22. D. K. Ferry, G. Edwards, K. Yamamoto, Y. Ochiai, J. Bird, K. Ishibashi, Y. Aoyagi, and T. Sugano, "Is There a Magnetic-Field-Induced Breakdown in the Universality of Conductance Fluctuations?" Japanese Journal of Applied Physics **34**, 4338-41 (1995).

23. D. K. Ferry, M. Khoury, D. P. Pivin, Jr., K. M. Connolly, T. K. Whidden, M. N. Kozicki, and D. R. Allee, "Nanolithography," Semiconductor Science and Technology B **11**, 1552-7 (1996).

24. D. K. Ferry and L. A. Akers, "Scaling Theory in Modern VLSI: Factors Affecting Interconnects, Wire Length, and Clock Speed," IEEE Circuit and Devices Magazine **13**(5), 41-4 (September 1997).

25. D. K. Ferry, R. Akis, and J. P. Bird, "Transmission in ballistic quantum dots," Superlattices and Microstructures **23**, 611-20 (1998).

26. D. K. Ferry and G. Edwards, "Studies of Chaotic Transport of Electrons in Quantum Boxes," VLSI Design **6**, 331-4 (1998).

27. A. Grincwajg, G. Edwards, and D. K. Ferry, "Conductance Fluctuations in Microstructures: Crossover between Different Transport Regimes," Physica B **218**, 92-96 (1996).

28. A. Grincwajg and D. K. Ferry, "Magnetotransport in corrugated quantum wires," Superlattices and Microstructures **20**, 331-6 (1996).

29. A. Grincwajg, D. K. Ferry, and G. Edwards, "Conductance Fluctuations in Quantum Wire Systems: A Comparison Between Scattering Models," Physica B **227**, 54-6 (1996).

30. A. Grincwajg, G. Edwards, and D. K. Ferry, "Quasi-Ballistic Transport in Quantum Point Contact Systems: A Comparison Between Different Scattering Models," Journal of Physics: Condensed Matter **9**, 673-84 (1997).

31. A. Grincwajg and D. K.Ferry, "Magnetotransport in Corrugated Quantum Wires," Physical Review B **55**, 7680 (1997).

32. H. L. Grubin, J. R. Caspar, and D. K. Ferry, "Phase space boundary conditions, dissipation, and quantum device transport," Physica Status Solidi (b) **204**, 365-7 (1997).

33. H. L. Grubin, and D. K. Ferry, "Interfaces, phase space boundaries and quantum device transport," Semiconductor Science and Technology **13**, A44-6 (1998).

34. H. L. Grubin, J. R. Caspar, and D. K. Ferry, "Phase space boundary conditions and quantum device transport," VLSI Design **8**, 215-8 (1998).

35. A. H. M. Kamal, M. J. Rack, M. N. Kozicki, D. K. Ferry, J. Lützen, and J. A. Hallmark, "Ultrathin cobalt silicide layers formed by rapid thermal processing of metal on amorphous silicon," Journal of Vacuum Science and Technology B **15**, 899-902 (1997).

36. A. H. M. Kamal, J. Lützen, B. A. Sanborn, M. V. Sidorov, M. N. Kozicki, D. J. Smith, and D. K. Ferry, "Two terminal nanocrystalline silicon memory device at room temperature," Semiconductor Science and Technology **13**, 1328-32 (1998).

37. M. Khoury and D. K. Ferry, "Effect of Molecular Weight on PMMA Resolution," Journal of Vacuum Science and Technology B 14, 75-9 (1996).

38. M. Khoury, A. Gunther, D. P. Pivin, Jr., M. J. Rack, and D. K. Ferry, "A Silicon Quantum Dot in a MOSFET Structure," Japanese Journal of Applied Physics **38**, 469-72 (1999).

39. M. Khoury, M. J. Rack, A. Gunther, and D. K. Ferry, "Spectroscopy of a silicon quantum dot," Applied Physics Letters **74**, 1576-8 (1999).

40. M. Khoury, D. P. Pivin, Jr., M. J. Rack, A. Gunther, and D. K. Ferry, "Fabrication of a Silicon Quantum Dot in a MOS Structure," Nanotechnology, in press.

41. M. D. Khoury, A. Gunther, M. J. Rack, D. P. Pivin, Jr., and D. K. Ferry, "Single Electron Effects in Silicon Quantum Dots in a MOSFET Structure," Microelectronics Journal, in press.

42. M. N. Kozicki, J. Allgair, D. K. Ferry, and T. K. Whidden, "The Use of Electron Beam Exposure and Chemically Enhanced Vapor Etching of SiO_2 for Nanoscale Fabrication," Physica B **227**, 318-22 (1996).

43. J. Lützen, A. H. M. Kamal, M. N. Kozicki, D. K. Ferry, M. V. Sidorov, and D. J. Smith, "Characterization of ultrathin nanocrystalline silicon films formed by annealing amorphous silicon," Journal of Vacuum Science and Technology B **16**, 2802-5 (1998).

44. J. Lützen, A. H. M. Kamal, M. N. Kozicki, D. K. Ferry, M. V. Sidorov, and D. J. Smith, "Characterization of Ultrathin Nanocrystalline Silicon Films Formed by Annealing Amorphous Silicon," Nanotechnology, in press.

45. J. Lützen, A. H. M. Kamal, M. N. Kozicki, and D. K. Ferry, "CMOS Compatible Fabrication of Single Electron Device," Nanotechnology, in press.

46. M. J. Rack, A. D. Gunther, M. Khoury, D. Vasileska, D. K. Ferry, and M. V. Sidorov, "Compatibility of cobalt and chromium depletion gates with RPECVD gate oxide for silicon based nanostructures," Semiconductor Science and Technology **13**, A71-4 (1998).

47. M. J. Rack, D. Vasileska, D. K. Ferry, and M. Sidorov, "Surface roughness of SiO_2 from a remote microwave plasma enhanced chemical vapor deposition process," J. Vac. Sci. Technol. B **16**, 2165-70 (1998).

48. P. Thanikasalam, T. K. Whidden, and D. K. Ferry, "Oxidation of silicon (100): Experimental data versus a unified chemical model," Journal of Vacuum Science and Technology B **14**, 2840-4 (1996).

49. T. K. Whidden, J. Allgair, J. M. Ryan, M. N. Kozicki, and D. K. Ferry, "Catalyzed HF Vapor Etching of Silicon Dioxide for Micro- and Nanolithographic Mask," Journal of the Electrochemical Society **142**, 1199-1205 (1995).

50. T. K. Whidden, P. Thanikasalam, M. J. Rack, and D. K. Ferry, "The Initial Oxidation of Silicon (100): A Unified, Chemical Model for Thin and Thick Oxide Growth Rates and Interfacial Structure," Journal Vacuum Science and Technology **B13**, 1618-25 (1995).

51. T. K. Whidden, J. Allgair, A. Jenkins-Gray, M. Khoury, M. N. Kozicki, and D. K. Ferry, "Nanoscale Lithography with Electron Exposure of SiO_2 Resists," Japanese Journal of Applied Physics **34**, 4420-25 (1995).

52. T. K. Whidden, D. K. Ferry, M. N. Kozicki, E. Kim, A. Kumar, J. Wilbur, and G. M. Whitesides, "Pattern Transfer to Silicon by Microcontact Printing and RIE," Nanotechnology **7**, 447-451 (1996).

53. M. Yazdani, D. K. Ferry, and L. A. Akers, "Interconnection Pin-outs for Today's Microprocessors," IEEE Circuit and Devices Magazine **13**(2), 28-31 March 1997.